Available online at www.sciencedirect.com
ScienceDirect
Comput. Methods Appl. Mech. Engrg. 412 (2023) 116077
Computer methods in applied mechanics and engineering
www.elsevier.com/locate/cma

A robust fifth order finite difference Hermite WENO scheme for compressible Euler equations☆

Chuan Fan[a], Zhuang Zhao[b,*], Tao Xiong[c], Jianxian Qiu[c]

[a] School of Mathematical Sciences, Xiamen University, Xiamen, Fujian 361005, PR China

[b] School of Mathematical Sciences and Institute of Natural Sciences, Shanghai Jiao Tong University, Shanghai 200240, PR China

[c] School of Mathematical Sciences and Fujian Provincial Key Laboratory of Mathematical Modeling and High-Performance Scientific Computing, Xiamen University, Xiamen, Fujian 361005, PR China

Received 15 January 2023; received in revised form 18 April 2023; accepted 19 April 2023
Available online 5 May 2023

Abstract

In this paper, we develop a robust fifth order finite difference Hermite weighted essentially non-oscillatory (HWENO) scheme for compressible Euler equations following the HWENO with limiter (HWENO-L) scheme (Zhang and Zhao, 2023). The HWENO-L scheme reduced storage and increased efficiency by using restricted derivatives only for time discretizations. However, it cannot control spurious oscillations well when facing strong shocks since the derivatives are directly used in spatial discretizations without any restrictions. To address such an issue, our proposed HWENO scheme performs flux reconstructions in the finite difference framework without using the derivative value of a target cell, which can result in a simpler and more robust scheme. The resulting scheme is simpler while achieving fifth order accuracy, making it more efficient. Besides, numerically we find it is very robust for some extreme problems even without positivity-preserving limiters. The proposed scheme also inherits advantages of previous HWENO schemes, including arbitrary positive linear weights in flux reconstructions, compact reconstructed stencils, and high resolution. Extensive numerical tests are performed to demonstrate the fifth order accuracy, efficiency, robustness, and high resolution of the proposed HWENO scheme.

MSC: 65M60; 35L65

Keywords: Finite difference scheme; Hermite WENO; Compressible Euler equations; Hyperbolic conservation laws; Positivity-preserving

☆ The research was partially supported by National Key R&D Program of China (Grant Number 2022YFA1004500) and Postdoctoral Science Foundation of China (Grant Number 2021M702145).

* Corresponding author.
E-mail addresses: fanchuan@stu.xmu.edu.cn (C. Fan), zzhao-m@sjtu.edu.cn (Z. Zhao), txiong@xmu.edu.cn (T. Xiong), jxqiu@xmu.edu.cn (J. Qiu).

https://doi.org/10.1016/j.cma.2023.116077
0045-7825/

1. Introduction

In this paper, we develop a robust finite difference (FD) Hermite weighted essentially non-oscillatory (HWENO) scheme to solve compressible Euler equations

$$\frac{\partial}{\partial t}\begin{bmatrix}\rho\\ \rho\mathbf{u}\\ E\end{bmatrix}+\nabla\cdot\begin{bmatrix}\rho\mathbf{u}\\ \rho\mathbf{u}\otimes\mathbf{u}+p\,\mathbb{I}\\ (E+p)\mathbf{u}\end{bmatrix}=0, \tag{1.1}$$

with the equation of state $p=(\gamma-1)\rho e$, where ρ is the density, $\mathbf{u}=(u,v)^T$ is the velocity, the superscript T denotes the transpose of a vector, E is the total energy given by $E=\frac{p}{\gamma-1}+\frac{1}{2}\rho\|\mathbf{u}\|^2$, p is the pressure, e is the internal energy, $\mathbb{I}$ is the identity matrix, $\|\mathbf{u}\|$ is the L_2 norm of vector $\mathbf{u}$, and γ is the ratio of specific heat (e.g., $\gamma=1.4$ for the ideal gas). The eigenvalues of Jacobian matrix for the flux functions are $\mathbf{u}-c$, $\mathbf{u}$, and $\mathbf{u}+c$, which involve the speed of sound $c=\sqrt{\gamma p/\rho}$. It is important to preserve the positivity of the density ρ and the pressure p. High order positivity-preserving (PP) schemes are widely studied for solving compressible Euler equations, including polynomial scaling and parametrized flux limiting approaches. We refer to [1] for reviewing the two approaches.

In past decades, a variety of high order numerical schemes, such as the finite difference (FD) schemes [2–6], finite volume (FV) schemes [7–11], and discontinuous Galerkin (DG) methods [12–16], have been developed to solve hyperbolic conservation laws and related problems. Among them, HWENO schemes are an important type of WENO schemes based on Hermite interpolations, which have been developed well in the past two decades. The FV HWENO schemes were first proposed by Qiu and Shu in [17,18] to evolve the Eqs. (1.1) and its first order derivative equations, simultaneously, which were initially used as limiters for DG methods. However, the two-dimensional HWENO scheme [18] cannot well control oscillations near strong shocks, such as that in the double Mach and forward step problems. Since the first order derivative used in the HWENO scheme [18] becomes quite large around strong shocks, it would lead to numerical oscillations and cause numerical instabilities. To overcome such an issue, Zhu and Qiu [19] designed another two-dimensional HWENO scheme by choosing a different stencil to approximate the first order derivative. Later, Capdeville [20] developed a FV Hermite upwind WENO scheme for solving hyperbolic conservation laws. Liu and Qiu [21] constructed a FD HWENO scheme by using an additional PP flux limiter [22]. Cai et al. employed a polynomial scaling PP limiter [23] to construct a PP FV HWENO scheme [24]. Tao et al. [25] constructed a FV central HWENO scheme on staggered meshes. Besides, Zahran and Abdalla generalized the fifth order FD HWENO scheme [21] to a seventh order FD HWENO scheme [26]. Ma and Wu [27] developed a compact HWENO scheme by using compact difference methods to approximate derivative values. Inspired from the DG method [12], Zhao et al. [28] proposed a high order FV hybrid HWENO scheme by updating both cell average values and first order moments with nonlinear HWENO reconstructions around discontinuities while using linear approximations in smooth regions. It had been extended to a FD framework [29]. Wibisono et al. [30] presented a fifth order FV Hermite targeted ENO scheme for hyperbolic conservation laws. Li et al. [31] proposed a class of high order FV and FD multi-resolution HWENO schemes from the idea of multi-resolution WENO methods [6]. Zhang and Zhao [32] developed a HWENO with limiter (HWENO-L) scheme to reduce storage and increase the efficiency of [29]. More explicitly, the restricted derivatives are both applied to time stages and flux reconstructions in [29], while they are only used to time discretizations in [32]. However, the HWENO-L scheme cannot simulate the one-dimensional Sedov and Leblanc problems even using PP limiters. The reason is that the HWENO-L scheme uses unrestricted derivative values in flux reconstructions, which are quite large near discontinuities. Compared with WENO schemes, the main advantage of HWENO schemes is that they are compact with a small stencil due to Hermite reconstructions. For example, a fifth order FD WENO scheme has full stencils with five points, while are only three for a same order HWENO scheme.

To conquer the shortcomings and retain the merits of the HWENO-L scheme [32], we develop a robust fifth order FD HWENO (HWENO-R) scheme to solve one- and two-dimensional compressible Euler equations. The derivative value of a target cell is no longer used in flux reconstructions for the HWENO-R scheme, which results in a simpler and more robust scheme. Several advantages of the proposed HWENO scheme are given below. Firstly, it still achieves fifth order accuracy in one- and two-dimensional cases by using less information in flux reconstructions. Secondly, unlike previous FD HWENO schemes [21,26,29,31,32], the order of accuracy for flux reconstructions is the same as that of the final scheme, which is more concise and has fewer computation cost. Thirdly, it is more robust as it performs well for many extreme problems without PP limiters, except for a few two-dimensional high

extreme problems, such as the 2000 Mach number astrophysical jet problem. Besides, it possesses the advantages of the HWENO-L scheme, including arbitrary positive linear weights in flux reconstructions, compact reconstructed stencils, and high resolution. Compared with WENO schemes in the same order, the proposed HWENO-R scheme has minor numerical errors and higher resolution. However, solving additional derivative equations would require more storage and computational cost. In the HWENO-R scheme, we use only linear approximations for the derivative equations to save computational cost while using a HWENO limiter for derivative values that appeared in each time stage for high order Runge–Kutta time discretizations. Numerically we find that spurious oscillations can be well controlled. To preserve the positivity of density and pressure, two PP FV HWENO schemes [24,33] were developed by using polynomial rescaling approaches [23,34]. Here, we take a parametrized PP flux limiting approach in [35] for two-dimensional high extreme problems since it allows larger time steps in practice and is more convenient for FD schemes.

The remainder of the paper is organized as follows. In Section 2, we describe detailed implementations of the HWENO-R scheme in one- and two-dimensional cases. In Section 3, numerical tests are performed to verify the fifth order accuracy, robustness, and high-resolution of the proposed scheme. Concluding remarks are given in Section 4.

2. Robust HWENO scheme

In this section, we present a fifth order FD HWENO-R scheme for one- and two-dimensional compressible Euler equations. Compared with the previous FD HWENO schemes [21,26,29,31,32], the HWENO-R scheme no longer uses the derivative of a target cell in flux reconstructions, which is simpler and more efficient as the HWENO-R scheme still achieves fifth order accuracy even using less information. The HWENO-R scheme is also more robust as it can simulate many extreme problems without any additional PP limiters.

2.1. HWENO-R reconstructions in one dimension

Firstly, a scalar hyperbolic conservation law in the one-dimensional case is considered as

$$u_t + f(u)_x = 0, \quad u(x,0) = u_0(x). \tag{2.1}$$

For the FD HWENO scheme in [21], it introduces an auxiliary variable $v = u_x$, and aims to solve

$$\begin{cases} u_t + f(u)_x = 0, & u(x,0) = u_0(x), \\ v_t + h(u,v)_x = 0, & v(x,0) = v_0(x), \end{cases} \tag{2.2}$$

where $h(u,v) = f(u)_x = f'(u)v$ and $v_0(x) = u_x(x,0) = u_0'(x)$. We consider a uniform mesh of a given spatial domain $[a,b]$ with grid points $\{x_i\}_{i=0}^{N_x}$, and the mesh size is $\Delta x = x_{i+1} - x_i$. x_i and $x_{i+\frac{1}{2}} = x_i + \Delta x/2$ are the center and interface of the cell $I_i = [x_i - \Delta x/2, x_i + \Delta x/2]$, respectively. With such, a conservative semi-discrete FD HWENO scheme for (2.2) is defined as

$$\begin{cases} \dfrac{\mathrm{d}u_i(t)}{\mathrm{d}t} = -\dfrac{1}{\Delta x}(\hat{f}_{i+\frac{1}{2}} - \hat{f}_{i-\frac{1}{2}}) \triangleq \mathcal{F}_i(u,v), \\ \dfrac{\mathrm{d}v_i(t)}{\mathrm{d}t} = -\dfrac{1}{\Delta x}(\hat{h}_{i+\frac{1}{2}} - \hat{h}_{i-\frac{1}{2}}) \triangleq \mathcal{H}_i(u,v), \end{cases} \tag{2.3}$$

where $\mathcal{F}_i(u,v)$ and $\mathcal{H}_i(u,v)$ are right-hand terms, and $\hat{f}_{i+\frac{1}{2}}$ and $\hat{h}_{i+\frac{1}{2}}$ are numerical fluxes given as

$$\hat{f}_{j+\frac{1}{2}} = \hat{f}\left(u_{j-r}, \ldots, u_{j+s}, v_{j-r}, \ldots, v_{j+s}\right), \quad \hat{h}_{j+\frac{1}{2}} = \hat{h}\left(u_{j-r}, \ldots, u_{j+s}, v_{j-r}, \ldots, v_{j+s}\right),$$

with a stencil at $\{x_{j-r}, \ldots, x_{j+s}\}$. Two implicit functions $\xi(x)$ and $\eta(x)$ are defined as that in [2,21], having

$$f(u) = \frac{1}{\Delta x}\int_{I_i} \xi(x)dx, \quad h(u,v) = \frac{1}{\Delta x}\int_{I_i} \eta(x)dx.$$

Since

$$f(u)_x = \frac{\xi(x+\Delta x/2) - \xi(x-\Delta x/2)}{\Delta x}, \quad h(u,v)_x = \frac{\eta(x+\Delta x/2) - \eta(x-\Delta x/2)}{\Delta x},$$

$\hat{f}_{i+\frac{1}{2}}$ and $\hat{h}_{i+\frac{1}{2}}$ are the approximations of $\xi(x_{i+\frac{1}{2}})$ and $\eta(x_{i+\frac{1}{2}})$, respectively. If $\hat{f}_{i+\frac{1}{2}}$ and $\hat{h}_{i+\frac{1}{2}}$ are high order approximations and Lipschitz continuous concerning their arguments, the right sides of (2.3) are high order approximations to $-f(u)_x$ and $-h(u,v)_x$ at $x = x_i$, respectively.

For a general flux, an upwind biasing technique is commonly used for stability by splitting the fluxes $f(u)$ and $h(u,v)$ into two parts: $f(u) = f^+(u) + f^-(u)$ and $h(u,v) = h^+(u,v) + h^-(u,v)$, with $\frac{\mathrm{d}f^+(u)}{\mathrm{d}u} \geq 0$ and $\frac{\mathrm{d}f^-(u)}{\mathrm{d}u} \leq 0$, $\frac{\partial h^+(u,v)}{\partial v} \geq 0$ and $\frac{\partial h^-(u,v)}{\partial v} \leq 0$, respectively. A global Lax–Friedrichs splitting approach is $f^{\pm}(u) = \frac{1}{2}(f(u) \pm \alpha u)$ and $h^{\pm}(u,v) = \frac{1}{2}(h(u,v) \pm \alpha v)$, where $\alpha = \max_u |f'(u)|$ and the maximum is taken in the global range of u.

Now we will give detailed HWENO-R reconstructions of $f^+(u)$ and $h^+(u,v)$ at point $x_{i+1/2}$, denoted as $\hat{f}^+_{i+\frac{1}{2}}$ and $\hat{h}^+_{i+\frac{1}{2}}$. The reconstructions of $\hat{f}^-_{i+\frac{1}{2}}$ and $\hat{h}^-_{i+\frac{1}{2}}$ are in a mirror symmetric with respect to $x_{i+\frac{1}{2}}$. For simplicity, the values of $f^+(u)$ and $h^+(u,v)$ at a point x_{i+k} are denoted as f^+_{i+k} and h^+_{i+k}, respectively.

- **Step I**. Obtain a quartic polynomial $q_0(x)$ based on $\{f^+_{i-1}, f^+_i, f^+_{i+1}, h^+_{i-1}, h^+_{i+1}\}$ by a Hermite reconstruction, satisfying

$$\frac{1}{\Delta x}\int_{I_l} q_0(x)dx = f^+_l, l = i-1, i, i+1 \quad \text{and} \quad \frac{1}{\Delta x}\int_{I_l} q_0'(x)dx = h^+_l, l = i-1, i+1,$$

and reconstruct two linear polynomials $q_1(x)$ and $q_2(x)$ based on $\{f^+_{i-1}, f^+_i\}$ and $\{f^+_i, f^+_{i+1}\}$, respectively, satisfying

$$\frac{1}{\Delta x}\int_{I_l} q_1(x)dx = f^+_l, l = i-1, i \quad \text{and} \quad \frac{1}{\Delta x}\int_{I_l} q_2(x)dx = f^+_l, l = i, i+1.$$

The main difference of our stencils as compared to the previous FD HWENO schemes [21,26,29,31,32] is that the stencils no longer contain the value of h^+_i, which will be explained afterward. Then we get the values of $q_0(x)$, $q_1(x)$, $q_2(x)$, and $q_0'(x)$ at the point $x_{i+\frac{1}{2}}$, namely,

$$\begin{aligned}
q_0(x_{i+\frac{1}{2}}) &= -\frac{23}{120}f^+_{i-1} + \frac{19}{30}f^+_i + \frac{67}{120}f^+_{i+1} - \Delta x(\frac{3}{40}h^+_{i-1} - \frac{7}{40}h^+_{i+1}),\\
q_1(x_{i+\frac{1}{2}}) &= \frac{3}{2}f^+_i - \frac{1}{2}f^+_{i-1},\\
q_2(x_{i+\frac{1}{2}}) &= \frac{1}{2}f^+_i + \frac{1}{2}f^+_{i+1},
\end{aligned}$$

and

$$q_0'(x_{i+\frac{1}{2}}) = \frac{1}{8\Delta x}(3f^+_{i-1} - 16f^+_i + 13f^+_{i+1}) + \frac{1}{8}h^+_{i-1} - \frac{3}{8}h^+_{i+1}.$$

- **Step II**. Compute smoothness indicators $\beta_k, k = 0, 1, 2$ as in [2], which measure the smoothness of the functions $q_k(x)$ in the cell I_i, satisfying

$$\beta_k = \sum_{\ell=1}^{r}\int_{I_i} \Delta x^{2\ell-1}(\frac{\mathrm{d}^\ell q_k(x)}{\mathrm{d}x^\ell})dx, k = 0, 1, 2, \tag{2.4}$$

where r is the degree of the polynomials $q_k(x)$. The explicit expressions are

$$\begin{cases}
\beta_0 = \frac{1}{16}\left[3(f^+_{i-1} - f^+_{i+1}) + \left(h^+_{i-1} + h^+_{i+1}\right)\Delta x\right]^2 + \frac{781}{320}\left[f^+_{i-1} - f^+_{i+1} + \left(h^+_{i-1} + h^+_{i+1}\right)\Delta x\right]^2\\
\qquad + \frac{1}{3900}\left[131(f^+_{i-1} - 2f^+_i + f^+_{i+1}) + 33\left(h^+_{i-1} - h^+_{i+1}\right)\Delta x\right]^2\\
\qquad + \frac{1421461}{36400}\left[2(f^+_{i-1} - 2f^+_i + f^+_{i+1}) + \left(h^+_{i-1} - h^+_{i+1}\right)\Delta x\right]^2,\\
\beta_1 = (f^+_{i-1} - f^+_i)^2,\\
\beta_2 = (f^+_i - f^+_{i+1})^2.
\end{cases}$$

- **Step III**. Compute nonlinear weights based on linear weights and smoothness indicators. As in the WENO scheme denoted by Zhu and Qiu (WENO-ZQ) [5], we also define a new parameter τ to measure the absolute

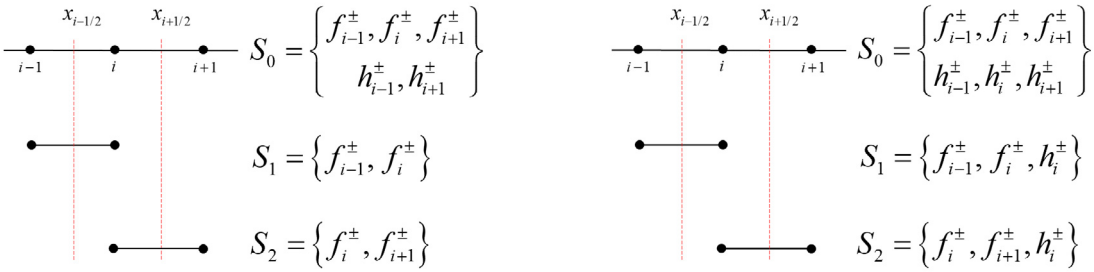

(a) HWENO-R scheme (b) HWENO-L scheme [32]

Fig. 2.1. Comparison of stencils used in HWENO flux reconstructions.

difference between β_0, β_1, and β_2 as

$$\tau = (\frac{|\beta_0 - \beta_1| + |\beta_0 - \beta_2|}{2})^2.$$

Then we compute the nonlinear weights by

$$\omega_k = \frac{\widetilde{\omega}_k}{\widetilde{\omega}_1 + \widetilde{\omega}_2 + \widetilde{\omega}_3}, \quad \text{with} \quad \widetilde{\omega}_k = \gamma_k(1 + \frac{\tau}{\beta_k + \varepsilon}), k = 0, 1, 2,$$

where ε is a small positive number to prevent zero denominators set to be 10^{-10} in this paper, and $\gamma_k, k = 0, 1, 2$ are the linear weights. By using Taylor expansions for f^+ and h^+ in β_k at smooth regions and the assumption of $\varepsilon \ll \beta_k$, we have $\frac{\tau}{\beta_k+\varepsilon} = \mathcal{O}(\Delta x^4), k = 0, 1, 2$. So the nonlinear weights $\omega_k = \gamma_k + \mathcal{O}(\Delta x^4), k = 0, 1, 2$ satisfy the accuracy condition to achieve a fifth order scheme [3,4].

- **Step IV**. Finally, following the idea of the HWENO-L [31,32] and WENO-ZQ [5] schemes, we use a nonlinear HWENO reconstruction to approximate $\hat{f}^+_{i+\frac{1}{2}}$, and adopt a linear approximation for $\hat{h}^+_{i+\frac{1}{2}}$ by the same quartic polynomial q_0, having

$$\begin{cases} \hat{f}^+_{i+1/2} = \omega_0 \left(\frac{1}{\gamma_0} q_0(x_{i+\frac{1}{2}}) - \frac{\gamma_1}{\gamma_0} q_1(x_{i+\frac{1}{2}}) - \frac{\gamma_2}{\gamma_0} q_2(x_{i+\frac{1}{2}}) \right) + \omega_1 q_1(x_{i+\frac{1}{2}}) + \omega_2 q_2(x_{i+\frac{1}{2}}), \\ \hat{h}^+_{i+\frac{1}{2}} = q_0'(x_{i+\frac{1}{2}}), \end{cases} \tag{2.5}$$

where $\gamma_k, k = 0, 1, 2$ can be arbitrary positive linear weights as long as $\gamma_0 + \gamma_1 + \gamma_2 = 1$. Numerically we find that the linear reconstruction of $\hat{h}^+_{i+\frac{1}{2}}$ works well without spurious oscillations.

Remark 2.1. Compared with the most relevant HWENO-L scheme [32], the derivative v_i (corresponding to h_i^+) at x_i is no longer used in the flux reconstructions of Step I. To distinguish the differences clearly, the sketch of HWENO flux reconstruction stencils is compared in Fig. 2.1. We find that the HWENO-L scheme directly uses unrestricted $h^{\pm}(u_i, v_i)$, which is a natural idea to use all available information. However, v_i might become quite large, especially for some extreme problems from our numerical investigations shown in Fig. 3.9, which makes the HWENO-L scheme less robust. Besides, with all available information, a sixth order reconstruction is used but only achieves fifth order accuracy for the final HWENO-L scheme, which is not optimal. Such shortages also exist in other FD HWENO schemes [21,26,29,31]. The proposed HWENO-R reconstruction is more robust, as it can directly simulate many extreme problems without any PP approaches. It is also optimal since the order of reconstructions is the same as that of the final scheme.

2.2. Runge–Kutta time discretizations

After spatial discretizations, we solve the semi-discrete scheme (2.3) by the following third order strong stability preserving (SSP) Runge–Kutta method

$$\begin{cases} \begin{bmatrix} u_i^{(1)} \\ v_i^{(1)} \end{bmatrix} = \begin{bmatrix} u_i^n \\ v_i^{n,lim} \end{bmatrix} + \Delta t \begin{bmatrix} \mathcal{F}_i(u^n, v^n) \\ \mathcal{H}_i(u^n, v^n) \end{bmatrix}, \\ \begin{bmatrix} u_i^{(2)} \\ v_i^{(2)} \end{bmatrix} = \frac{3}{4} \begin{bmatrix} u_i^n \\ v_i^{n,lim} \end{bmatrix} + \frac{1}{4} \left(\begin{bmatrix} u_i^{(1)} \\ v_i^{(1),lim} \end{bmatrix} + \Delta t \begin{bmatrix} \mathcal{F}_i(u^{(1)}, v^{(1)}) \\ \mathcal{H}_i(u^{(1)}, v^{(1)}) \end{bmatrix} \right), \\ \begin{bmatrix} u_i^{n+1} \\ v_i^{n+1} \end{bmatrix} = \frac{1}{3} \begin{bmatrix} u_i^n \\ v_i^{n,lim} \end{bmatrix} + \frac{2}{3} \left(\begin{bmatrix} u_i^{(2)} \\ v_i^{(2),lim} \end{bmatrix} + \Delta t \begin{bmatrix} \mathcal{F}_i(u^{(2)}, v^{(2)}) \\ \mathcal{H}_i(u^{(2)}, v^{(2)}) \end{bmatrix} \right), \end{cases} \tag{2.6}$$

where $v_i^{n,lim}$, $v_i^{(1),lim}$ and $v_i^{(2),\ lim}$ are the restricted derivatives of v_i^n, $v_i^{(1)}$ and $v_i^{(2)}$ by a HWENO limiter described below. As was shown in previous FD HWENO schemes [29,32], these derivatives might become quite large near discontinuities. Here following [29,32], we also restrict the derivatives only for the values appeared in the time stages as shown in (2.6).

In the following, we will briefly introduce the procedures of a HWENO limiter to restrict $\{v_i^n, v_i^{(1)}, v_i^{(2)}\}$ and obtain $\{v_i^{n,lim}, v_i^{(1),lim}, v_i^{(2),lim}\}$ correspondingly, which are denoted as $\{u_i^{\#}, v_i^{\#}, v_i^{\#,lim}\}$ for $\# = n, (1), (2)$. We will apply a Hermite interpolation based on $\{u_{i-1}^{\#}, u_i^{\#}, u_{i+1}^{\#}, v_{i-1}^{\#}, v_{i+1}^{\#}\}$ to obtain a quartic polynomials $p_0(x)$, and use linear interpolations based on $\{u_{i-1}^{\#}, u_i^{\#}\}$ and $\{u_i^{\#}, u_{i+1}^{\#}\}$ to get two linear polynomials $p_1(x)$, $p_2(x)$, respectively. For simplicity, we drop the super index # below, and we have

$$\begin{cases} p_0(x): \ p_0(x_l) = u_l, l = i-1, i, i+1, \ p_0'(x_l) = v_l, l = i-1, i+1, \\ p_1(x): \ p_1(x_l) = u_l, l = i-1, i, \\ p_2(x): \ p_2(x_l) = u_l, l = i, i+1. \end{cases}$$

We compute smoothness indicators $\hat{\beta}_k(x)$ as in (2.4) to measure the smoothness of the functions $p_k(x)$, and the expressions are

$$\begin{cases} \hat{\beta}_0 = \frac{1}{1600} \left[29(u_{i-1} - u_{i+1}) + 9\,(v_{i-1} + v_{i+1})\,\Delta x\right]^2 \\ \qquad + \frac{781}{320} \left[u_{i-1} - u_{i+1} + (v_{i-1} + v_{i+1})\,\Delta x\right]^2 \\ \qquad + \frac{1}{191100} \left[787(u_{i-1} - 2u_i + u_{i+1}) + 166\,(v_{i-1} - v_{i+1})\,\Delta x\right]^2 \\ \qquad + \frac{1421461}{36400} \left[2(u_{i-1} - 2u_i + u_{i+1}) + (v_{i-1} - v_{i+1})\,\Delta x\right]^2, \\ \hat{\beta}_1 = (u_i - u_{i-1})^2, \\ \hat{\beta}_2 = (u_i - u_{i+1})^2. \end{cases}$$

We also define a parameter $\hat{\tau}$ to measure the absolute difference between $\hat{\beta}_0$, $\hat{\beta}_1$ and $\hat{\beta}_2$ as

$$\hat{\tau} = \left(\frac{|\hat{\beta}_0 - \hat{\beta}_1| + |\hat{\beta}_0 - \hat{\beta}_2|}{2} \right)^2,$$

and the nonlinear weights are defined as

$$\hat{\omega}_k = \frac{\overline{\omega}_k}{\overline{\omega}_1 + \overline{\omega}_2 + \overline{\omega}_3}, \quad \text{with} \quad \overline{\omega}_k = d_k \left(1 + \frac{\hat{\tau}}{\hat{\beta}_k + \varepsilon} \right), \quad k = 0, 1, 2,$$

where ε is also taken as 10^{-10}. Finally, the restricted derivative $v_i^{\#,lim}$ is obtained from

$$v_i^{\#,lim} = \hat{\omega}_0 \left(\frac{1}{d_0} p_0'(x_i) - \frac{d_1}{d_0} p_1'(x_i) - \frac{d_2}{d_0} p_2'(x_i) \right) + \hat{\omega}_1 p_1'(x_i) + \hat{\omega}_2 p_2'(x_i), \tag{2.7}$$

where $d_k, k = 0, 1, 2$ are arbitrary positive linear weights as long as their sum equals one, and the explicit expressions of $p_k'(x_i)$ can be found in [32]. Note that this limiter is only fifth order accurate, which is why the HWENO-L scheme cannot achieve sixth order accuracy.

2.3. HWENO-R reconstructions in two dimensions

A two-dimensional scalar hyperbolic conservation law is considered as

$$u_t + f(u)_x + g(u)_y = 0, \quad u(x, y, 0) = u_0(x, y). \tag{2.8}$$

Correspondingly, we introduce two auxiliary variables $v = u_x$ and $w = u_y$ as in [21], having

$$\begin{cases} u_t + f(u)_x + g(u)_y = 0, & u(x, y, 0) = u_0(x, y), \\ v_t + h(u, v)_x + r(u, v)_y = 0, & v(x, y, 0) = v_0(x, y), \\ w_t + q(u, w)_x + s(u, w)_y = 0, & w(x, y, 0) = w_0(x, y), \end{cases} \tag{2.9}$$

with

$$h(u, v) = f(u)_x = f'(u)v, \quad r(u, v) = g(u)_x = g'(u)v, \quad v_0(x, y) = u_x(x, y, 0),$$
$$q(u, w) = f(u)_y = f'(u)w, \quad s(u, w) = g(u)_y = g'(u)w, \quad w_0(x, y) = w_y(x, y, 0).$$

We consider a uniform mesh of a given domain $[a, b] \times [c, d]$ with grid points $\{(x_i, y_j)\}$ for $i = 0, \ldots, N_x$, $j = 0, \ldots, N_y$ with mesh sizes $\Delta x = x_{i+1} - x_i$ and $\Delta y = y_{j+1} - y_j$. (x_i, y_j) is the center of cell $I_{i,j} = [x_{i-\frac{1}{2}}, x_{i+\frac{1}{2}}] \times [y_{j-\frac{1}{2}}, y_{j+\frac{1}{2}}]$, with interfaces $x_{i+\frac{1}{2}} = x_i + \Delta x/2$ and $y_{j+\frac{1}{2}} = y_j + \Delta y/2$. A conservative semi-discrete FD HWENO scheme for (2.9) is defined as

$$\begin{cases} \dfrac{\mathrm{d}u_{i,j}(t)}{\mathrm{d}t} = -\dfrac{1}{\Delta x}(\hat{f}_{i+\frac{1}{2},j} - \hat{f}_{i-\frac{1}{2},j}) - \dfrac{1}{\Delta y}(\hat{g}_{i,j+\frac{1}{2}} - \hat{g}_{i,j-\frac{1}{2}}), \\ \dfrac{\mathrm{d}v_{i,j}(t)}{\mathrm{d}t} = -\dfrac{1}{\Delta x}(\hat{h}_{i+\frac{1}{2},j} - \hat{h}_{i-\frac{1}{2},j}) - \dfrac{1}{\Delta y}(\hat{r}_{i,j+\frac{1}{2}} - \hat{r}_{i,j-\frac{1}{2}}), \\ \dfrac{\mathrm{d}w_{i,j}(t)}{\mathrm{d}t} = -\dfrac{1}{\Delta x}(\hat{q}_{i+\frac{1}{2},j} - \hat{q}_{i-\frac{1}{2},j}) - \dfrac{1}{\Delta y}(\hat{s}_{i,j+\frac{1}{2}} - \hat{s}_{i,j-\frac{1}{2}}), \end{cases} \tag{2.10}$$

where the numerical fluxes $\{\hat{f}_{i\pm\frac{1}{2},j}, \hat{h}_{i\pm\frac{1}{2},j}\}$ are reconstructed along the x-direction with a fixed y and the numerical fluxes $\{\hat{g}_{i,j\pm\frac{1}{2}}, \hat{s}_{i,j\pm\frac{1}{2}}\}$ are reconstructed along the y-direction with a fixed x, by using the same HWENO reconstruction as described in Section 2.1.

Special attention should be paid to the numerical fluxes $\hat{q}_{i\pm\frac{1}{2},j}$ and $\hat{r}_{i,j\pm\frac{1}{2}}$, which approximate the mixed derivative terms $q_x = (f'(u)w)_x = f(u)_{xy}$ and $r_y = (g'(u)v)_y = g(u)_{xy}$, respectively. In [21,31], a third order reconstruction with a flux splitting is used, making $v_{i,j}(t)$ and $w_{i,j}(t)$ be only third order approximations. Instead, we directly use fourth order linear approximation to reconstruct $\hat{q}_{i+\frac{1}{2},j}$ and $\hat{r}_{i,j+\frac{1}{2}}$ as in [29,32], i.e.,

$$\begin{cases} \hat{q}_{i+\frac{1}{2},j} = -\frac{1}{12}q_{i-1,j} + \frac{7}{12}q_{i,j} + \frac{7}{12}q_{i+1,j} - \frac{1}{12}q_{i+2,j}, \\ \hat{r}_{i,j+\frac{1}{2}} = -\frac{1}{12}r_{i,j-1} + \frac{7}{12}r_{i,j} + \frac{7}{12}r_{i,j+1} - \frac{1}{12}r_{i,j+2}. \end{cases} \tag{2.11}$$

Then, the HWENO-R scheme achieves a fully fifth order accuracy and is much simpler, and numerically we find that such linear reconstructions for $\hat{q}_{i+\frac{1}{2},j}$ and $\hat{r}_{i,j+\frac{1}{2}}$ also work well.

Similarly to the 1D case, we use the explicit third order SSP Runge–Kutta method (2.6) to solve the semi-discrete HWENO scheme (2.10). To control spurious oscillations, the HWENO limiter (2.7) is also applied to modify $v^{\#}_{i,j}$ and $w^{\#}_{i,j}$ by a dimension-by-dimension methodology. Finally, $v^{\#,lim}_{i,j}$ and $w^{\#,lim}_{i,j}$ are obtained and only acted as time stage values too.

2.4. Algorithms of HWENO-R scheme

Remark 2.2. For one- and two-dimensional compressible Euler equations, it is important to perform HWENO reconstructions for numerical fluxes along local characteristic directions to control numerical oscillations around shocks and contact discontinuities. Besides, linear reconstructions of numerical fluxes in the derivative equations are implemented in each component.

Algorithm 1: one-dimensional case

Input: $\{u_i^n, v_i^n\}$ at time level n.
Output: $\{u_i^{n+1}, v_i^{n+1}\}$ at time level $n+1$.

Step I. Compute the right-hand terms of (2.3) for spatial discretizations.
for $i = 0, N_x$ **do**
  Compute $\hat{f}^+_{i+\frac{1}{2}}$ and $\hat{h}^+_{i+\frac{1}{2}}$ by (2.5), similarly for $\hat{f}^-_{i+\frac{1}{2}}$ and $\hat{h}^-_{i+\frac{1}{2}}$.
  Compute $\hat{f}_{i+\frac{1}{2}} = \hat{f}^+_{i+\frac{1}{2}} + \hat{f}^-_{i+\frac{1}{2}}$ and $\hat{h}_{i+\frac{1}{2}} = \hat{h}^+_{i+\frac{1}{2}} + \hat{h}^-_{i+\frac{1}{2}}$.
Step II. Compute restricted derivatives $v_i^{\#,lim}$ by (2.7).
Step III. Evolve to time level $n+1$ from time level n by (2.6).

Algorithm 2: two-dimensional case

Input: $\{u_{i,j}^n, v_{i,j}^n, w_{i,j}^n\}$ at time level n.
Output: $\{u_{i,j}^{n+1}, v_{i,j}^{n+1}, w_{i,j}^{n+1}\}$ at time level $n+1$.

Step I. Compute the right-hand terms of (2.10) for spatial discretizations.
for $j = 0, \ldots, N_y$, **do**
  for $i = 0, \ldots, N_x$, **do**
    Compute $\{\hat{f}_{i+\frac{1}{2},j}, \hat{h}_{i+\frac{1}{2},j}\}$ by one-dimensional reconstructions in Section 2.1.
    Compute the mixed derivative term $\hat{q}_{i+\frac{1}{2},j}$ by (2.11).
for $i = 0, \ldots, N_x$, **do**
  for $j = 0, \ldots, N_y$, **do**
    Compute $\{\hat{g}_{i,j+\frac{1}{2}}, \hat{s}_{i,j+\frac{1}{2}}\}$ by one-dimensional reconstructions in Section 2.1.
    Compute the mixed derivative term $\hat{r}_{i,j+\frac{1}{2}}$ by (2.11).
Step II. Compute restricted derivatives $v_{i,j}^{\#,lim}$ and $w_{i,j}^{\#,lim}$ by a dimension-by-dimension approach, which is similar to compute $v_i^{\#,lim}$ by (2.7).
Step III. Evolve to time level $n+1$ from time level n, similarly to (2.6).

Remark 2.3. For a few tough extreme tests of two-dimensional compressible Euler equations, such as Mach 2000 astrophysical jet flows and the shock reflection and diffraction problem, the proposed HWENO scheme cannot work without PP limiters due to the appearance of negative density and pressure. Since only a few 2D extreme situations require PP limiters, we will utilize a parametrized PP flux limiter [35] for 2D problems, which allows larger time steps in a relatively large CFL number and does not sacrifice accuracy. The parametrized PP flux limiter is very convenient for FD schemes, and the implementations are given in Appendix for 2D FD HWENO schemes.

Remark 2.4. For the additional derivative variable v, its boundary treatment depends on the main variable u. For periodic, reflective, and outflow boundary conditions, v uses the same boundary treatment as u. For other boundary conditions, such as Dirichlet or inflow boundary condition, we simply set v be 0.

3. Numerical tests

In this section, we will perform numerical tests in one- and two-dimensional cases to verify the fifth order accuracy, high resolution, and robustness of the proposed HWENO-R scheme. For comparisons, we mainly consider the HWENO-R, HWENO-L [32] and WENO-ZQ [5] schemes since the three schemes all use arbitrary positive linear weights in flux reconstructions. The linear weights of the HWENO-L and WENO-ZQ schemes are chosen as suggested from [5,32]. For the HWENO-R scheme, we take the linear weights $\{\gamma_0 = 0.99,\ \gamma_1 = \gamma_2 = 0.005\}$ in the flux reconstruction (2.5) and $\{d_0 = 0.9,\ d_1 = d_2 = 0.05\}$ in the limiter (2.7), based on our investigations in Example 3.4.

Table 3.1
Example 3.1. The L_1 errors, orders, and CPU time of the HWENO-R, HWENO-L, and WENO-ZQ schemes.

Mesh	HWENO-R			HWENO-L			WENO-ZQ		
	L_1 error	Order	CPU	L_1 error	Order	CPU	L_1 error	Order	CPU
10	2.55E−02	–	3.92E−05	1.66E−02	–	4.26E−05	1.67E−02	–	3.18E−05
20	3.24E−03	2.98	1.35E−04	1.13E−03	3.88	1.57E−04	1.47E−03	3.50	1.10E−04
40	1.32E−04	4.61	6.95E−04	2.40E−05	5.55	8.19E−04	7.34E−05	4.33	5.67E−04
80	1.04E−06	6.99	4.14E−03	5.04E−07	5.58	4.91E−03	2.40E−06	4.93	3.33E−03
160	1.47E−08	6.15	2.58E−02	1.07E−08	5.56	3.14E−02	7.15E−08	5.07	2.16E−02
320	3.69E−10	5.32	1.65E−01	3.24E−10	5.05	2.00E−01	2.12E−09	5.08	1.38E−01
10×10	2.80E−02	–	2.90E−04	2.34E−02	–	3.56E−04	1.83E−02	–	2.21E−04
20×20	4.04E−03	2.79	2.68E−03	6.09E−04	5.26	3.18E−03	1.80E−03	3.34	2.10E−03
40×40	4.54E−05	6.48	3.11E−02	1.26E−05	5.59	4.12E−02	7.47E−05	4.59	2.48E−02
80×80	1.09E−06	5.38	4.18E−01	5.04E−07	4.64	5.35E−01	2.41E−06	4.95	2.98E−01
160×160	1.46E−08	6.22	5.16E+00	1.07E−08	5.56	6.56E+00	7.12E−08	5.08	3.82E−00
320×320	3.64E−10	5.33	7.48E+01	3.20E−10	5.06	9.04E+01	2.10E−09	5.08	4.81E+01

To assess the efficiency and performance of these schemes, we first offer the results of accuracy tests. For the discontinuous tests, we only concentrate on comparing the HWENO-R and WENO-ZQ schemes in some extreme problems since the HWENO-L scheme cannot simulate even using PP limiters. We no longer present the comparative results of the classical WENO [2], WENO-ZQ, modified HWENO [29] and HWENO-L schemes, which were given in [32]. The PP researches of the classical WENO scheme were presented in [22,35,36].

Since HWENO schemes contain additional derivative equations, the boundary treatment of derivative variables can be seen in Remark 2.4. For time steps, in the one-dimensional case, we take $\Delta t = \mathrm{CFL}\,(\Delta x)^{\frac{5}{3}}/\Lambda$ for smooth problems to observe the orders of spatial accuracy, and $\Delta t = \mathrm{CFL}\,/(\Lambda/\Delta x)$ for other problems, where Λ is the spectral radius over the spatial domain for $\mathbf{F}(\mathbf{U})$, respectively. Correspondingly, in two-dimensional case, we take $\Delta t = \mathrm{CFL}/(\Lambda_x/(\Delta x)^{\frac{5}{3}} + \Lambda_y/(\Delta y)^{\frac{5}{3}})$ for smooth problems and $\Delta t = \mathrm{CFL}/(\Lambda_x/\Delta x + \Lambda_y/\Delta y)$ for others, where Λ_x and Λ_y are the spectral radiuses over spatial domains for $\mathbf{F}'(\mathbf{U})$ and $\mathbf{G}'(\mathbf{U})$, respectively. CFL is taken as 0.6 in our computations. For the comparison of computational cost, we run our simulations based on the programming language Fortran 95 on the environment Inter(R) Xeon (R) Gold 6130 CPU @ 2.10 GHz.

Example 3.1. We first consider the accuracy test of scalar conservation laws. One- and two-dimensional Burgers' equations are used to verify the fifth order accuracy and compare computational efficiency for the HWENO-R, HWENO-L, and WENO-ZQ schemes. In the 1D case, the initial condition is $u(x, 0) = 0.5 + \sin(\pi x)$ with periodic boundary conditions in the domain $[0, 2]$. In the 2D case, the initial condition is $u(x, y, 0) = 0.5 + \sin(\pi(x + y)/2)$ with periodic boundary conditions in the domain $[0, 4] \times [0, 4]$. Their final time T is $0.5/\pi$ when the solutions are smooth. The L_1 norm of numerical errors for the three schemes are given in Table 3.1, which shows the schemes all achieve fifth order accuracy. More explicitly, in the 1D case with denser meshes (e.g., ≥ 160), the CPU time ratio of HWENO-R/WENO-ZQ is about 1.195, whereas the error ratio is around 1/5.263, and the CPU time ratio of HWENO-L/WENO-ZQ is around 1.452, but the error ratio is almost 1/6.623. In the 2D case with denser meshes (e.g., $\geq 160 \times 160$), the CPU time ratio of HWENO-R/WENO-ZQ is about 1.453, whereas the error ratio is around 1/5.291, and the CPU time ratio of HWENO-L/WENO-ZQ is almost 1.798, but the error ratio is around 1/6.623. These data demonstrate that at the same CPU cost, the HWENO schemes are more accurate than the WENO-ZQ scheme as the product of the CPU time ratio and the error ratio is less than 1. More intuitively, the L_1 errors and CPU time measured in seconds are plotted in Fig. 3.1, which shows that the HWENO-R and HWENO-L schemes are more efficient than the WENO-ZQ scheme for the HWENO schemes obtain minor errors on the fixed CPU time as the mesh gets denser. Besides, the HWENO-R scheme is slightly more efficient than the HWENO-L scheme even though they have similar numerical errors, which illustrates that some numerical wastes exist in flux reconstructions of the HWENO-L scheme.

Example 3.2. We consider an accuracy test of the HWENO-R, HWENO-L, and WENO-ZQ schemes for one-dimensional compressible Euler equations to compare computational efficiency. The initial condition is

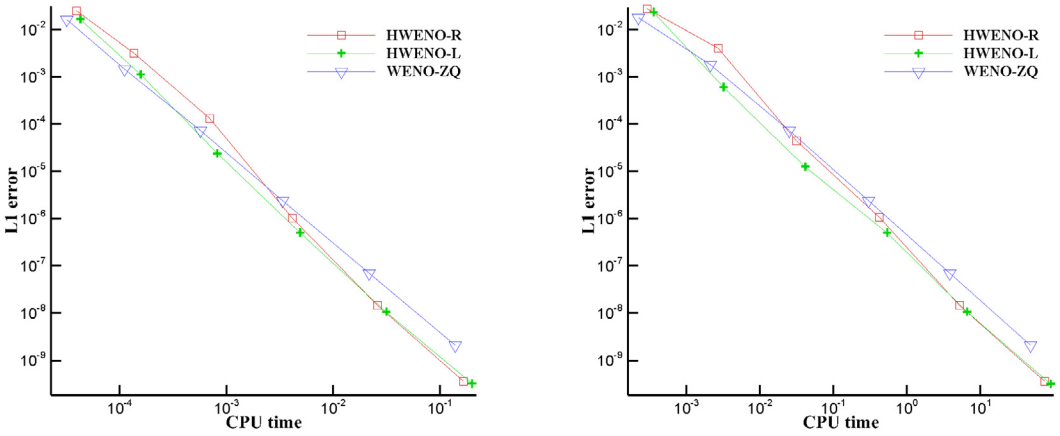

(a) 1D Burgers' equation (b) 2D Burgers' equation

Fig. 3.1. Comparison of L_1 errors and CPU time for Example 3.1.

Table 3.2
Example 3.2. The L_1 errors, orders, and CPU time of the HWENO-R, HWENO-L, and WENO-ZQ schemes.

Mesh	HWENO-R			HWENO-L			WENO-ZQ		
	L_1 error	Order	CPU	L_1 error	Order	CPU	L_1 error	Order	CPU
10	6.00E−03	–	2.70E−03	1.63E−03	–	3.34E−03	3.47E−03	–	2.34E−03
20	3.57E−04	4.07	1.28E−02	3.50E−05	5.54	1.51E−02	8.72E−05	5.31	9.68E−03
40	1.78E−06	7.65	7.71E−02	6.94E−07	5.65	9.07E−02	2.88E−06	4.92	5.78E−02
80	1.68E−08	6.73	4.80E−01	1.53E−08	5.51	5.71E−01	9.13E−08	4.98	3.71E−01
160	4.80E−10	5.13	3.04E+00	4.80E−10	4.99	3.61E+00	2.87E−09	4.99	2.34E−00
320	1.51E−11	5.00	1.95E+01	1.51E−11	5.00	2.32E+01	9.01E−11	5.00	1.49E+01

$(\rho, u, p, \gamma) = (1 + 0.2\sin(\pi x), 1, 1, 1.4)$ with periodic boundary conditions in the domain $[0, 2]$. Up to the final time $T = 2$, the exact solutions are $(\rho, u, p) = (1 + 0.2\sin(\pi(x - T)), 1, 1)$. The numerical errors and CPU time of the HWENO-R, HWENO-L, and WENO-ZQ schemes are presented in Table 3.2, which shows the three schemes all achieve fifth order accuracy. More explicitly, on the denser meshes (e.g., ≥ 80), the CPU time ratio of HWENO-R/WENO-ZQ is about 1.301, whereas the error ratio is around 1/5.780, and the CPU time ratio of HWENO-L/WENO-ZQ is almost 1.546, but the error ratio is around 1/5.988. These data demonstrate that at the same CPU cost, the HWENO schemes are more accurate than the WENO-ZQ scheme, which also can be known from Fig. 3.2, where the L_1 errors and CPU time measured in seconds are plotted. Obviously, the HWENO schemes obtain minor errors than the WENO-ZQ scheme on the fixed CPU time as the mesh gets denser, and the HWENO-R scheme is also slightly more efficient than the HWENO-L scheme.

Example 3.3 (*Accuracy test for the isentropic vortex evolution problem*)**.** We consider the isentropic vortex problem [36] for 2D compressible Euler equations to test the order of spatial accuracy with PP limiters. For this problem, the background flow is $\rho = p = u = v = 1$. We add a perturbation of an isentropic vortex centered at (x_0, y_0) to the velocity field (u, v) and temperature $T = p/\rho$, with a constant entropy $S = p/\rho^\gamma$, that is,

$$(\delta u, \delta v) = \frac{\epsilon}{2\pi} e^{0.5(1-r^2)}(-\bar{y}, \bar{x}), \quad \delta T = \frac{(\gamma - 1)\epsilon^2}{8\gamma\pi^2} e^{1-r^2}, \tag{3.1}$$

where $(\bar{x}, \bar{y}) = (x - x_0, y - y_0)$, $r^2 = \bar{x}^2 + \bar{y}^2$. The computational domain is a square of $[-5, 15]^2$ and $(x_0, y_0) = (5, 5)$, with periodic boundary conditions. Here $\gamma = 1.4$ and the vortex strength $\epsilon = 10.0828$. The exact solution is a passive convection of the vortex with respect to the mean velocity. The lowest density and pressure of the exact

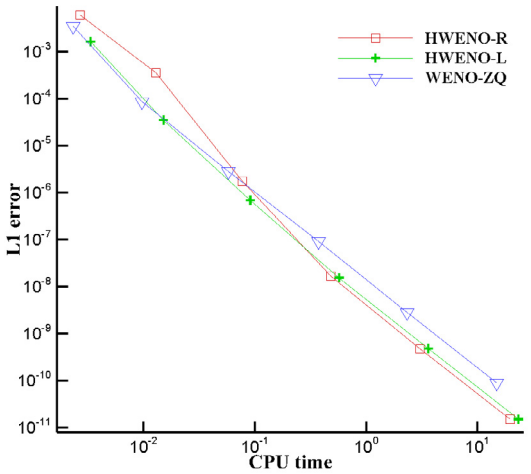

(a) 1D Euler equations

Fig. 3.2. Comparison of L_1 errors and CPU time for Example 3.2.

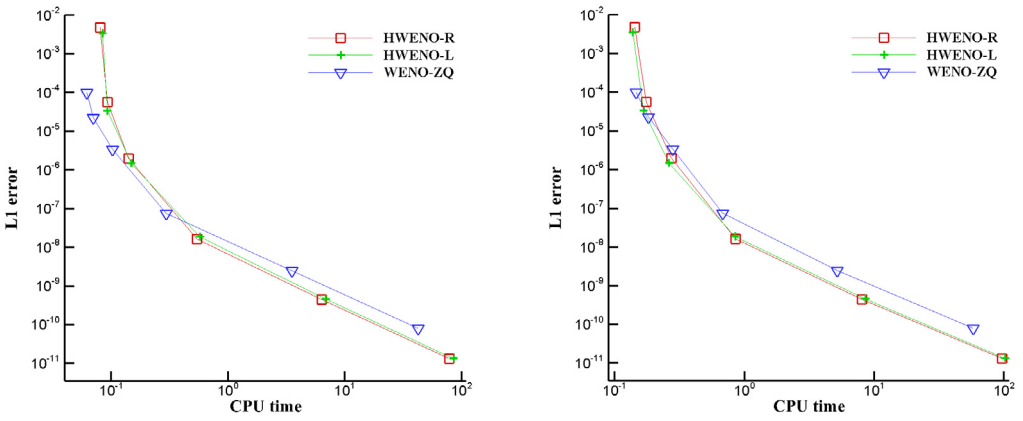

(a) Without PP limiter (b) With PP limiter

Fig. 3.3. Comparison of L_1 errors and CPU time for Example 3.3.

solutions are 7.8×10^{-15} and 1.7×10^{-20}, respectively. The final time is $T = 0.01$ for the HWENO-R, HWENO-L, and WENO-ZQ schemes. The L_1 errors, orders of accuracy, and CPU time are presented in Table 3.3, which shows that the three schemes achieve desired fifth order accuracy, without or with the PP limiters. More explicitly, on the denser meshes (e.g., $\geq 320 \times 320$), the CPU time ratios of HWENO-R/WENO-ZQ without and with PP limiters are about 1.823 and 1.609, respectively, whereas the error ratios are almost 1/5.524, and the CPU time ratios of HWENO-L/WENO-ZQ without and with PP limiters are almost 1.978 and 1.704, respectively, but the error ratios are around 1/5.682. These data demonstrate that at the same CPU cost, the HWENO schemes are more accurate than the WENO-ZQ scheme. From Fig. 3.3, we can see more intuitive results, in which the L_1 errors and CPU time are plotted. Then, we can know that the HWENO-R and HWENO-L schemes are more efficient than the WENO-ZQ scheme without or with PP limiters as the mesh gets denser. Besides, the HWENO-R scheme is slightly more efficient than the HWENO-L scheme by using less CPU time.

Table 3.3
Example 3.3. The L_1 errors, orders, and CPU time of the HWENO-R, HWENO-L, and WENO-ZQ schemes. WO: without PP limiters; WL: with PP limiters.

Mesh	WO					WL				
	L_1 error	Order	ρ_{min}	p_{min}	CPU	L_1 error	Order	ρ_{min}	p_{min}	CPU
HWENO-R										
20 × 20	1.24E−03	–	3.43E−02	9.43E−03	8.00E−02	1.24E−03	–	3.43E−02	9.43E−03	1.43E−01
40 × 40	1.32E−04	3.23	1.94E−03	−1.90E−03	9.30E−02	1.32E−04	3.23	3.33E−03	1.00E−13	1.75E−01
80 × 80	6.58E−06	4.32	8.51E−05	9.82E−06	1.41E−01	6.58E−06	4.32	8.51E−05	9.82E−06	2.74E−01
160 × 160	4.78E−08	7.11	5.39E−06	1.73E−06	5.43E−01	4.78E−08	7.11	5.39E−06	1.73E−06	8.50E−01
320 × 320	4.78E−10	6.64	2.55E−07	2.95E−08	6.33E−00	4.78E−10	6.64	2.55E−07	2.95E−08	8.03E−00
640 × 640	1.34E−11	5.16	1.22E−08	4.67E−10	7.87E+01	1.34E−11	5.16	1.22E−08	4.67E−10	9.66E+01
HWENO-L										
20 × 20	3.38E−03	–	3.10E−01	−1.55E+00	8.42E−02	3.51E−03	–	2.14E−01	8.52E−02	1.38E−01
40 × 40	3.40E−05	6.64	1.01E−04	−8.04E−04	9.23E−02	3.40E−05	6.69	8.77E−04	1.00E−13	1.67E−01
80 × 80	1.48E−06	4.52	6.69E−05	9.98E−06	1.48E−01	1.48E−06	4.52	6.69E−05	9.98E−06	2.62E−01
160 × 160	1.87E−08	6.31	1.09E−05	1.83E−06	5.74E−01	1.87E−08	6.31	1.09E−05	1.83E−06	8.48E−01
320 × 320	4.57E−10	5.36	4.81E−07	3.13E−08	6.86E−00	4.57E−10	5.36	4.81E−07	3.13E−08	8.53E−00
640 × 640	1.34E−11	5.09	1.23E−08	4.80E−10	8.55E+01	1.34E−11	5.09	1.23E−08	4.80E−10	1.02E+02
WENO-ZQ										
20 × 20	1.01E−04	–	4.99E−04	−4.94E−03	6.14E−02	1.01E−04	–	1.83E−03	9.99E−14	1.46E−01
40 × 40	2.25E−05	2.16	−1.92E−04	5.14E−04	7.03E−02	2.32E−05	2.11	8.86E−04	1.00E−13	1.82E−01
80 × 80	3.47E−06	2.70	3.66E−04	−2.65E−04	1.03E−01	3.46E−06	2.75	2.47E−04	1.68E−05	2.80E−01
160 × 160	7.64E−08	5.50	1.70E−05	1.31E−05	2.96E−01	7.64E−08	5.50	1.70E−05	1.31E−05	6.80E−01
320 × 320	2.48E−09	4.95	1.16E−06	2.80E−07	3.53E−00	2.48E−09	4.95	1.16E−06	2.80E−07	5.17E−00
640 × 640	7.96E−11	4.96	6.93E−08	4.93E−09	4.25E+01	7.96E−11	4.96	6.93E−08	4.93E−09	5.80E+01

Remark 3.1. From Tables 3.1–3.3, we can see that the order of HWENO-R, HWENO-L and WENO-ZQ schemes is less or greater than five, or the HWENO-L scheme might have minor errors than the HWENO-R scheme on coarser meshes. But, the three schemes achieve the designed fifth order accuracy, and the HWENO-R and HWENO-L schemes have similar numerical errors as the mesh gets denser. The reason is that when we compute the convergence rates, we usually assume the truncation errors for a fifth order scheme are of the form Ch^5, where C is a constant that does not depend on the mesh size h. However, this is only true when h is small enough. For coarse meshes, the truncation errors might not be exactly of the form Ch^5, so we could observe those phenomenons above.

Example 3.4. We now solve the blast wave problem modeled by one-dimensional compressible Euler equations. The initial condition is

$$(\rho, u, p, \gamma) = \begin{cases} (1, 0, 1000, 1.4), & \text{if } x \in [0, 0.1), \\ (1, 0, 0.01, 1.4), & \text{if } x \in [0.1, 0.9), \\ (1, 0, 100, 1.4), & \text{if } x \in [0.9, 1], \end{cases} \tag{3.2}$$

with reflective boundary conditions on the left and right. The final time is $T = 0.038$. The reference solution is generated by the classical WENO scheme [2] using 2001 points. For the HWENO-R, HWENO-L and WENO-ZQ schemes, the computational density is plotted in Fig. 3.4, which shows the HWENO-R and HWENO-L schemes have higher resolution than the WENO-ZQ scheme due to compact spatial stencils. Meanwhile, the HWENO-R scheme uses less information in flux reconstructions but has slightly better resolution than the HWENO-L scheme.

Next, we will investigate the linear weights $\{\gamma_0, \gamma_1, \gamma_2\}$ for flux reconstructions in (2.5) and $\{d_0, d_1, d_2\}$ for HWENO limiter in (2.7) on how they affect the results of the HWENO-R scheme. For simplicity, the HWENO-R scheme with those given linear weights in Table 3.4 is denoted as HWENO-R:(Dk,Gk).

Firstly, for the fixed linear weights $D1$ in the limiter, the comparative results computed by the HWENO-R scheme with linear weights $\{G1, G2, G3, G4\}$ are shown in Fig. 3.5. We can see that the resolution of the solution is affected by the linear weights in the flux reconstructions, and larger γ_0 with the fixed $D1$ may result in better resolution. Secondly, for the fixed $G1$ in the flux reconstructions, we also give the computational results of HWENO-R with

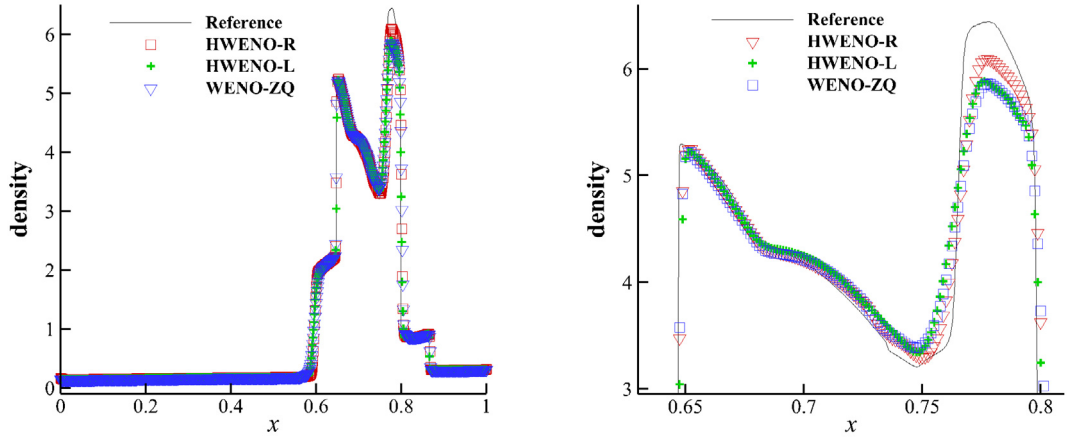

(a) density with 800 meshes. (b) A zoomed-in figure

Fig. 3.4. Example 3.4. The results of solution computed by the HWENO-R, HWENO-L and WENO-ZQ schemes for the blast wave problem.

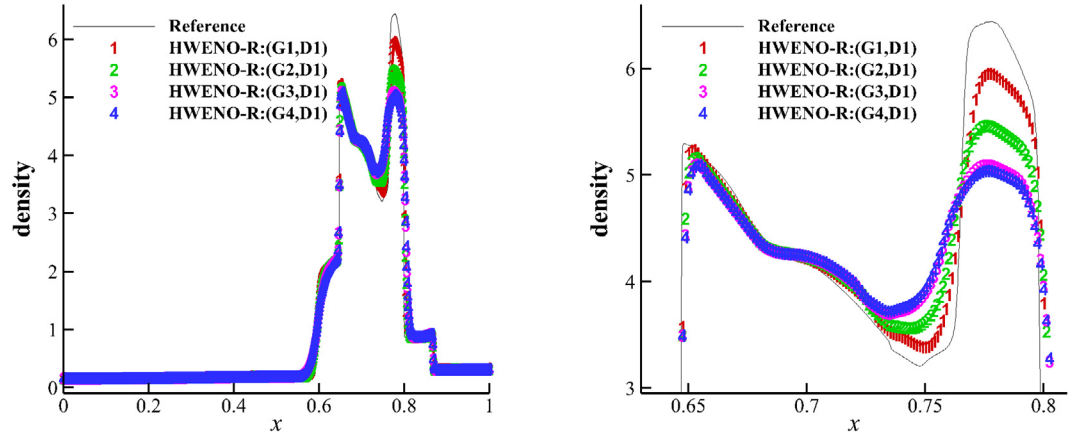

(a) Fixed $D1$ in limiter (b) A zoomed-in figure

Fig. 3.5. Example 3.4. The results of solution computed by the HWENO-R schemes with different linear weights in the flux reconstructions and fixed $D1$ in the limiter.

the linear weights $\{D1, D2, D3, D4\}$ in Fig. 3.6. Then, we know that the resolution of the solution is also affected by the linear weights in the limiter, and larger or smaller d_0 with the fixed $G1$ may result in worse resolution.

To control spurious oscillations and obtain better resolutions, γ_0 and d_0 cannot be set quite large or small in the flux reconstructions and limiter. By trial and error, if the linear weights $\frac{\gamma_0}{\gamma_1} \in [100, 300]$ and $\frac{d_0}{d_1} \in [10, 30]$ are used in the flux reconstructions and the limiting process, respectively, the results obtained by the HWENO-R scheme are similar with high resolution and non-oscillation, shown in Fig. 3.7. Taking a compromise option, we recommend adopting the linear weights $\{G1, D2\}$ in the flux reconstructions and limiting process, that is $\{\gamma_0 = 0.99,\ \gamma_1 = \gamma_2 = 0.005\}$ in (2.5) and $\{d_0 = 0.9,\ d_1 = d_2 = 0.05\}$ in (2.7). For other numerical tests of this paper, the HWENO-R scheme with the recommended linear weights can control numerical oscillations well, behaving with high resolution in simulations.

Example 3.5. We solve the Sedov problem of one-dimensional compressible Euler equations, which involves low-density and strong shocks. The computational domain is $[-2, 2]$, the density is $\rho(x, 0) = 1$, the velocity

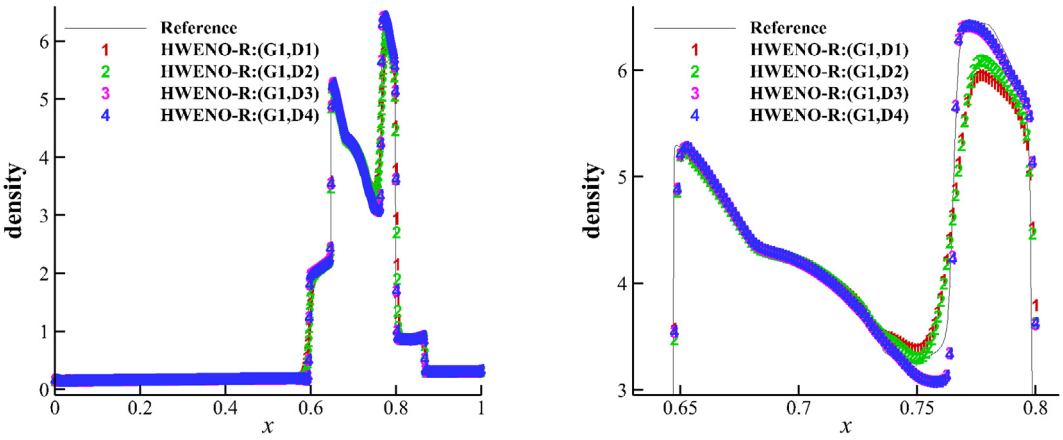

(a) Fixed $G1$ in flux reconstructions (b) A zoomed-in figure

Fig. 3.6. Example 3.4. The results of solution computed by the HWENO-R schemes with different linear weights in the limiter and fixed $G1$ in the flux reconstructions.

Table 3.4
Example 3.4. The HWENO-R:(Gk,Dk) schemes with different linear weights in the flux reconstructions and limiter.

In the flux reconstructions	In the limiter
$G1:\{\gamma_0=0.99,\gamma_1=\gamma_2=0.005\}$	$D1:\{d_0=0.99,d_1=d_2=0.005\}$
$G2:\{\gamma_0=0.9,\gamma_1=\gamma_2=0.05\}$	$D2:\{d_0=0.9,d_1=d_2=0.05\}$
$G3:\{\gamma_0=\gamma_1=\gamma_2=1/3\}$	$D3:\{d_0=d_1=d_2=1/3\}$
$G4:\{\gamma_0=0.1,\gamma_1=\gamma_2=0.45\}$	$D4:\{d_0=0.1,d_1=d_2=0.45\}$
$G5:\{\gamma_0=100/102,\gamma_1=\gamma_2=1/102\}$	$D5:\{d_0=10/12,d_1=d_2=1/12\}$
$G6:\{\gamma_0=150/152,\gamma_1=\gamma_2=1/152\}$	$D6:\{d_0=15/17,d_1=d_2=1/17\}$
$G7:\{\gamma_0=200/202,\gamma_1=\gamma_2=1/202\}$	$D7:\{d_0=20/22,d_1=d_2=1/22\}$
$G8:\{\gamma_0=250/252,\gamma_1=\gamma_2=1/252\}$	$D8:\{d_0=25/27,d_1=d_2=1/27\}$
$G9:\{\gamma_0=300/302,\gamma_1=\gamma_2=1/302\}$	$D9:\{d_0=30/32,d_1=d_2=1/32\}$

is $u(x,0)=0$, and the total energy is $E(x,0)=10^{-12}$ everywhere except in the center cell with a constant $E(x,0)=3.2\times10^6/\Delta x$. We take $\gamma=1.4$, and the final time is $T=0.001$. The exact solution is provided in [37,38]. Outflow boundary conditions are imposed on the left and right. The computational density are shown in Fig. 3.8, where the HWENO-R scheme with compact reconstructed stencils performs slightly better than the WENO-ZQ scheme. The HWENO-L scheme cannot simulate this problem even using the parametrized PP flux limiting approach in [35].

To investigate the reason of the failure in simulations for the HWENO-L scheme, we present the derivatives of density after marching one time step for the HWENO-R and HWENO-L schemes in Fig. 3.9. We can see that the derivatives of the HWENO-L scheme have more dramatic variations than the HWENO-R scheme. More explicitly, the maximum value of derivatives for density exceeds 4000 in the HWENO-L scheme, while less than 20 in the HWENO-R scheme. This phenomenon shows that huge numerical oscillations for density are existed in the HWENO-L scheme, leading to the failures of the HWENO-L scheme in the simulation as time evolves. Besides, this issue cannot be solved by using PP limiters as the PP limiters can keep the positivity of density and pressure but cannot control numerical oscillations. Conversely, the proposed HWENO-R scheme can well simulate this test without any PP limiters, which shows the strong robustness of the HWENO-R scheme.

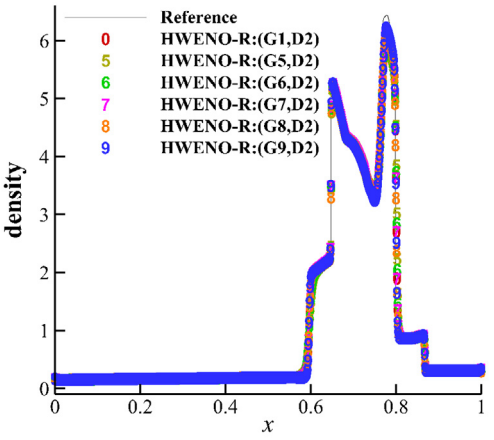

(a) $\frac{\gamma_0}{\gamma_1} \in [100, 300]$ with fixed $D2$

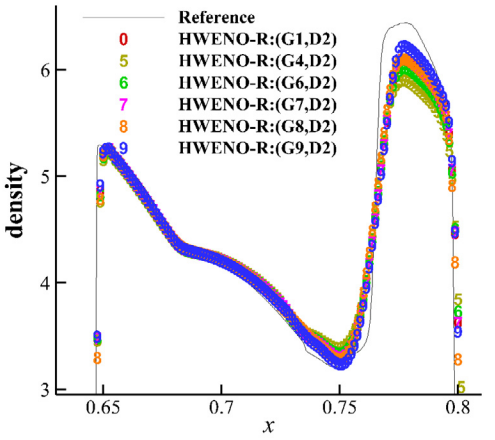

(b) A zoomed-in figure

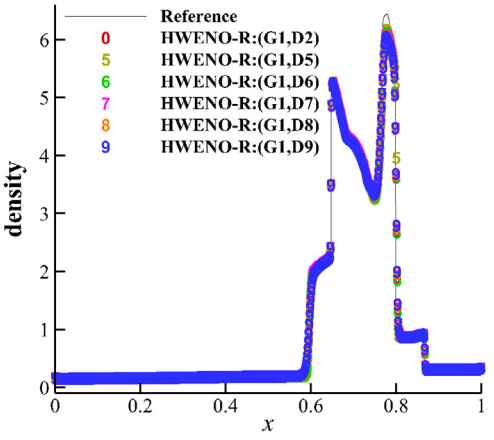

(c) $\frac{d_0}{d_1} \in [10, 30]$ with fixed $G1$

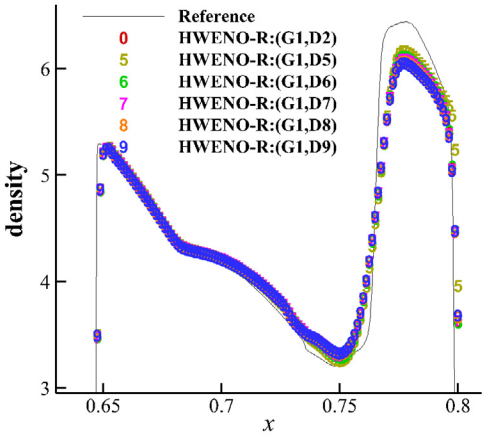

(d) A zoomed-in figure

Fig. 3.7. Example 3.4. The results of solution computed by the HWENO-R schemes.

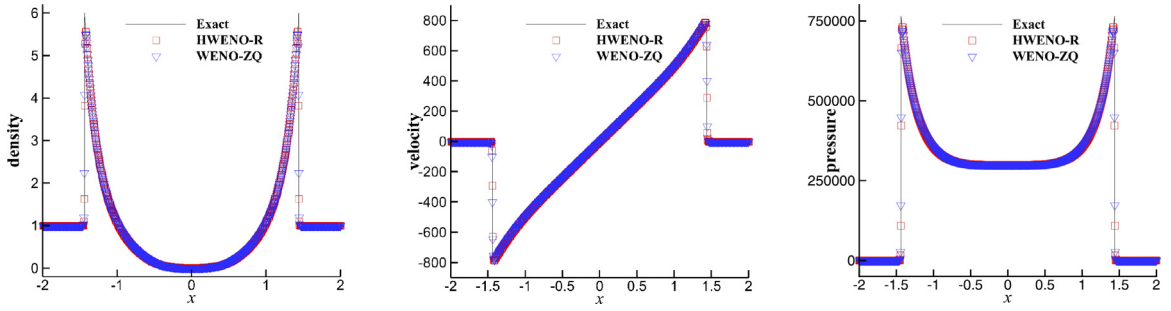

Fig. 3.8. Example 3.5. Sedov problem with 800 meshes.

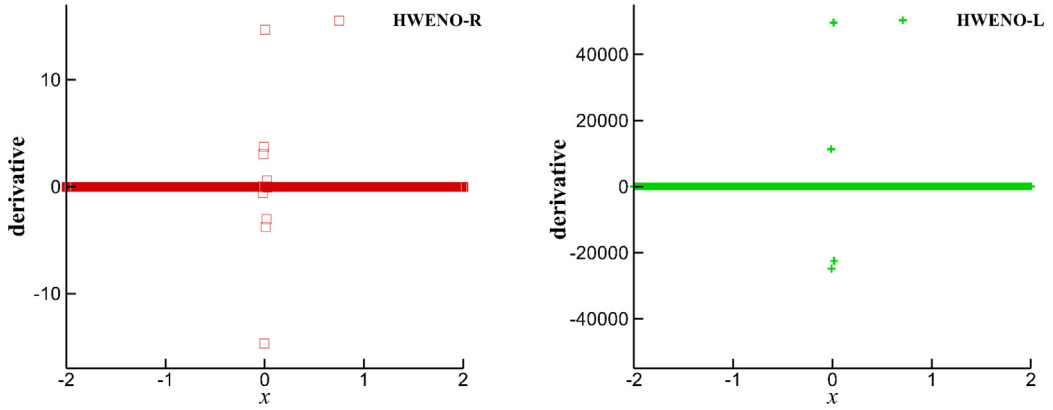

Fig. 3.9. Example 3.5. The comparison of the derivative of density after marching one time step for Sedov problem with 800 meshes.

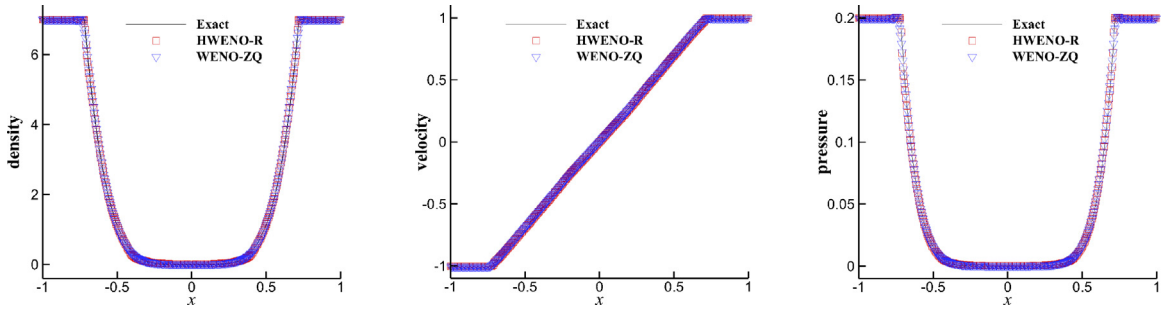

Fig. 3.10. Example 3.6. Double rarefaction problem with 400 meshes.

Example 3.6. We solve the double rarefaction problem [39] of one-dimensional compressible Euler equations, which includes low-density and low-pressure solutions. The initial condition is

$$(\rho, u, p, \gamma) = \begin{cases} (7, -1, 0.2, 1.4), & \text{if } x \in [-1, 0), \\ (7, 1, 0.2, 1.4), & \text{if } x \in [0, 1]. \end{cases} \tag{3.3}$$

Outflow boundary conditions are imposed on the left and right. The final time is $T = 0.6$. The results are shown in Fig. 3.10. The HWENO-R and WENO-ZQ schemes work well for this extreme problem without PP limiters, but the HWENO-R scheme has more compact reconstructed stencils.

Example 3.7. We solve the Leblanc problem of one-dimensional compressible Euler equations. The initial condition is

$$(\rho, u, p, \gamma) = \begin{cases} (2, 0, 10^9, 1.4), & \text{if } x \in [-10, 0), \\ (10^{-3}, 0, 1, 1.4), & \text{if } x \in [0, 10]. \end{cases} \tag{3.4}$$

Outflow boundary conditions are imposed on the left and right. The final time is $T = 0.0001$. We show the computational density in Fig. 3.11 for the HWENO-R and WENO-ZQ schemes without PP limiters. They can perform well in this case and have similar performances. The other FD HWENO schemes [21,26,29,31,32] cannot simulate the problem directly. The reconstructed stencils of the HWENO-R and HWENO-L schemes are more compact than the WENO-ZQ scheme, but the HWENO-L scheme also fails to simulate this extreme problem, even with PP limiters.

Example 3.8. We solve the double Mach reflection problem of two-dimensional compressible Euler equations. The computational domain is $[0, 4] \times [0, 1]$. The initial condition is a pure right-moving Mach 10 shock, initially

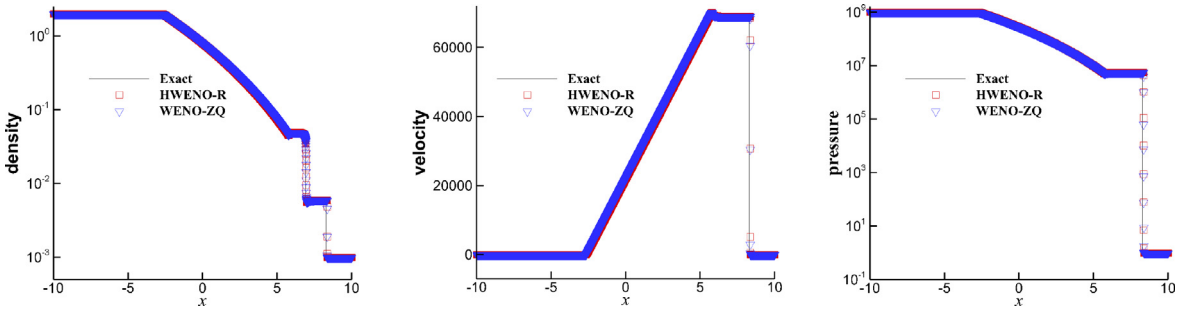

Fig. 3.11. Example 3.7. Leblanc problem with 6400 meshes.

located at $x = \frac{1}{6}$, $y = 0$, making a 60° angle with the x-axis. The left and right boundaries are inflow and outflow, respectively. The top boundary is the exact motion of a Mach 10 shock. For the bottom boundary, the exact post-shock condition is posed on $[0, \frac{1}{6}] \times \{0\}$, and a reflective boundary is used for the rest. The computational density in the final time $T = 0.2$ are showed in Fig. 3.12 for the HWENO-R, HWENO-L, and WENO-ZQ schemes. The HWENO-L and HWENO-R schemes can capture more complicated structures around the double Mach stems than the WENO-ZQ scheme because of using compact reconstructed stencils. The HWENO-R scheme also has a slightly higher resolution than the HWENO-L scheme, even using less information in flux reconstructions.

Example 3.9. We solve the forward step problem of two-dimensional compressible Euler equations containing a Mach 3 wind tunnel with a step. The computational domain is a union of $[0, 0.6] \times [0, 1]$ and $[0.6, 1] \times [0.2, 1]$. The initial condition is a right-going Mach 3 flow. Reflective boundary conditions are used along the wall of the tunnel. Inflow and outflow boundary conditions are used at the entrance and exit, respectively. The final time is $T = 4$. The results of computational density are shown in Fig. 3.13 for the HWENO-R, HWENO-L, and WENO-ZQ schemes. Due to more compact stencils, the HWENO-R and HWENO-L schemes have better resolution than the WENO-ZQ scheme, and the HWENO-R scheme has slightly higher resolution than the HWENO-L scheme. The total CPU time is 29093.92 s for the HWENO-R scheme, 31945.12 s for the HWENO-L scheme, and 20542.55 s for the WENO-ZQ scheme. Correspondingly, the CPU time ratios of HWENO-R/WENO-ZQ and HWENO-L/WENO-ZQ are around 1.416 and 1.555, respectively, which also show that the HWENO-R scheme has higher efficiency than the HWENO-L scheme. Besides, the two HWENO schemes use more CPU cost than the WENO-ZQ scheme, as the HWENO schemes bring additional derivative equations, but the HWENO schemes have slightly better resolutions with more compact stencils.

Example 3.10. We now consider a Sedov problem of two-dimensional compressible Euler equations. The computational domain is $[0, 1.1]^2$. For the initial condition, similarly to the 1D case, the density is $\rho(x, y, 0) = 1$, the velocities are $u(x, y, 0) = v(x, y, 0) = 0$, and the total energy is $E(x, y, 0) = 10^{-12}$ everywhere except on the lower left corner with a constant $E(x, y, 0) = \frac{0.244816}{\Delta x \Delta y}$. $\gamma = 1.4$. Reflective boundary conditions are used on the left and bottom, while outflow conditions are on the right and upper boundaries. The exact solution is provided in [37,38]. The final time is $T = 1$. The computational results of the HWENO-R and WENO-ZQ schemes are shown in Fig. 3.14. The two schemes without PP limiters work well for this test with capturing the front density propagation, and the HWENO-R scheme has slightly better resolution than the WENO-ZQ scheme due to more compact stencils. However, other existing FD HWENO schemes [21,26,29,31,32] fail to work for this problem directly.

Example 3.11. We solve the Mach 2000 astrophysical jet problem without a radiative cooling, which has been studied in [40–42]. The computational domain is $[0, 1] \times [-0.25, 0.25]$. Initially, it is full of an ambient gas with $(\rho, u, v, p, \gamma) = (0.5, 0, 0, 0.4127, 5/3)$. We take outflow boundary conditions on the right, top, and bottom. On the left boundary, we set $(\rho, u, v, p) = (5, 800, 0, 0.4127)$, $y \in [-0.05, 0.05]$ and $(\rho, u, v, p) = (0.5, 0, 0, 0.4127)$ for

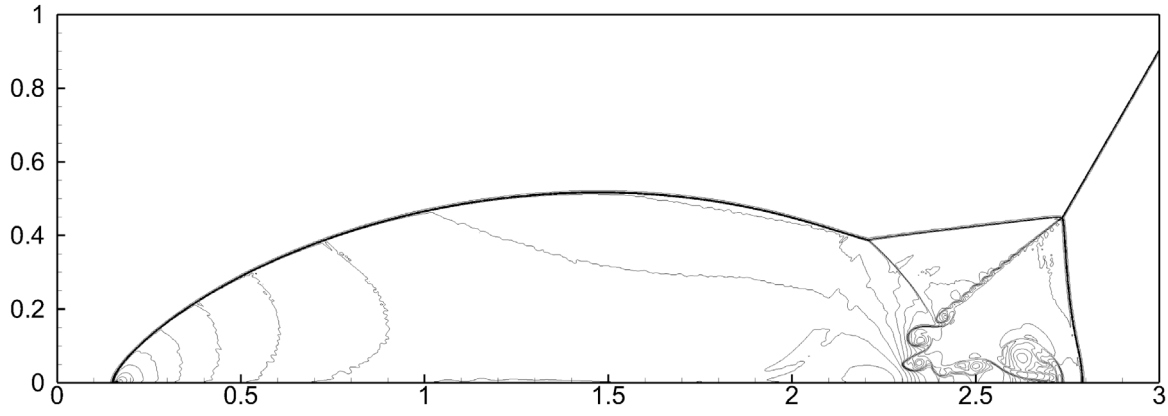

(a) HWENO-R

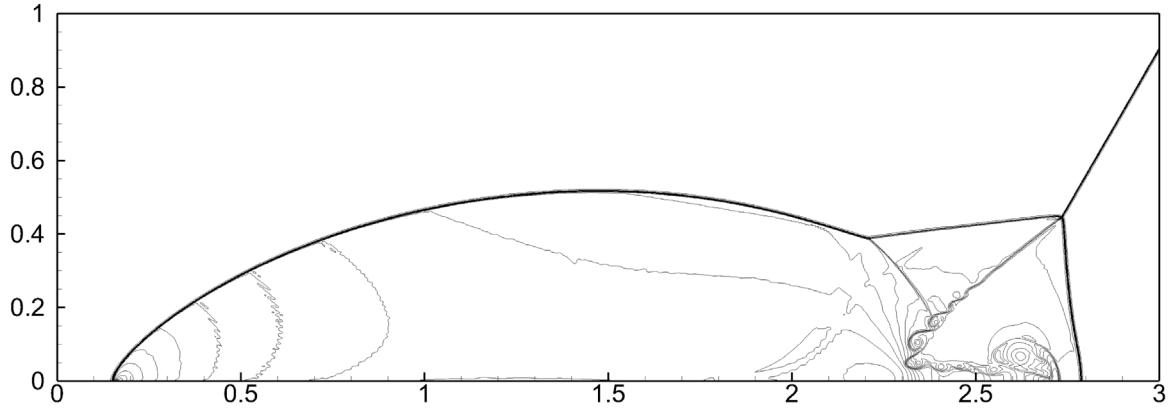

(b) HWENO-L

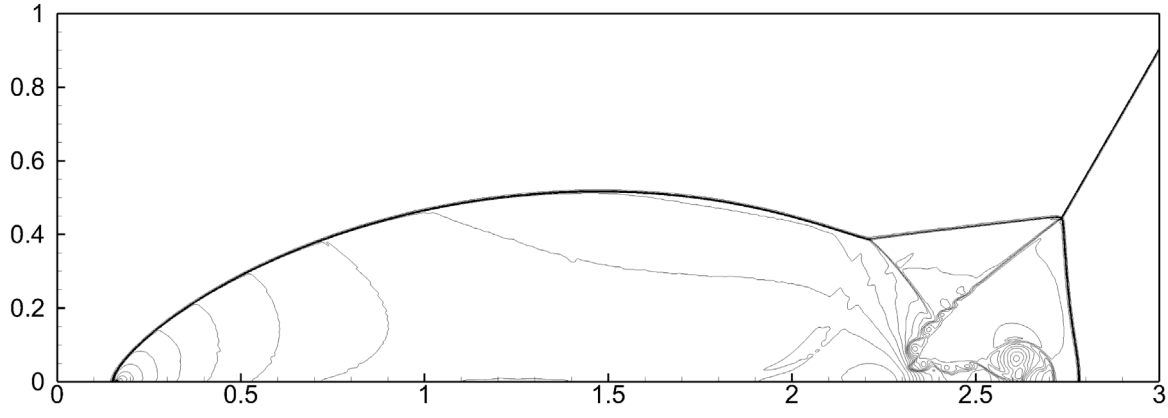

(c) WENO-ZQ

Fig. 3.12. Example 3.8. Double Mach reflection problem. Contour plots of density with 30 equally spaced lines from 1.5 to 22.7. Meshes: 1600×400.

the rest. The results of computational density in the final time $T = 0.001$ are shown in Fig. 3.15 for the HWENO-R and WENO-ZQ schemes, which cannot work without PP limiters. The HWENO-R scheme coupled with PP limiters

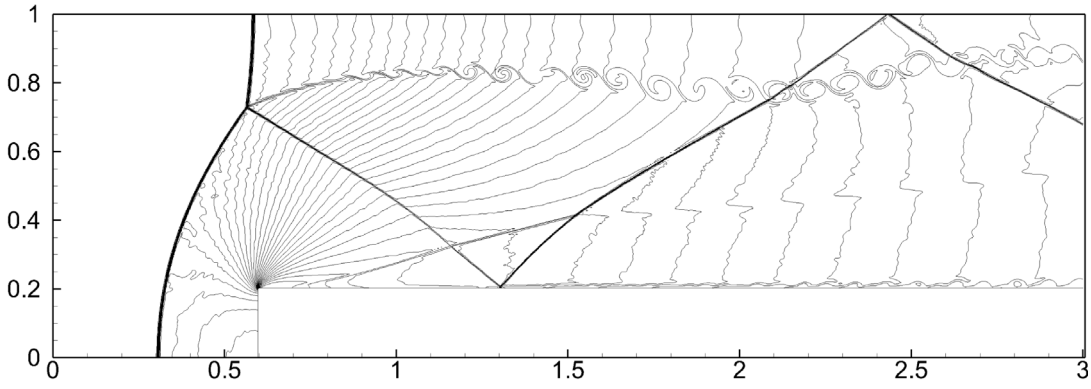

(a) HWENO-R

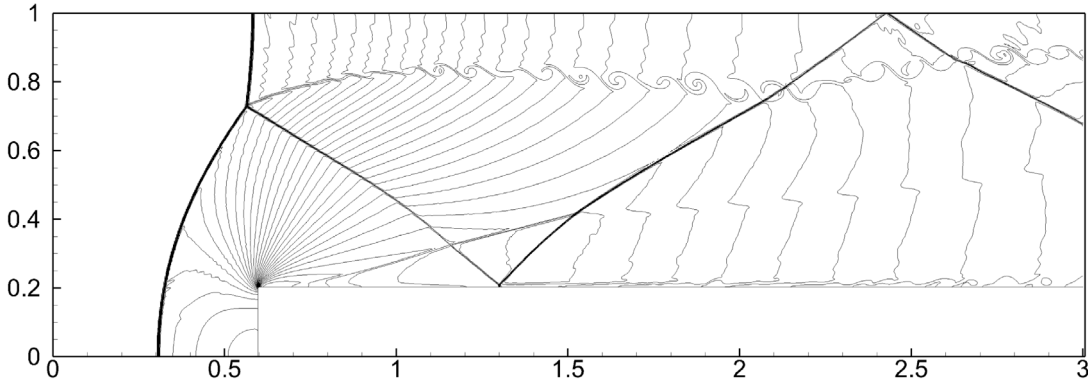

(b) HWENO-L

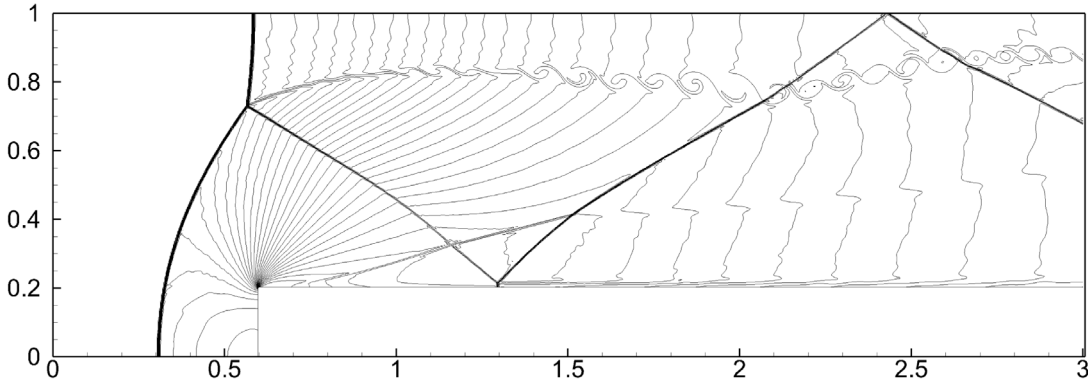

(c) WENO-ZQ

Fig. 3.13. Example 3.9. Forward step problem. Contour plots of density with 30 equally spaced lines from 0.32 to 6.15. Meshes: 960 × 320.

performs well for this problem, and the proportion of cells that used PP limiters is about 0.0146%, which has similar resolutions with the WENO-ZQ scheme. Besides, the total CPU time for the HWENO-R scheme is 2292.73 s, and the CPU time ratio of HWENO-R/WENO-ZQ is 1.577. It has an obvious difference compared with Example 3.9 since the PP limiters are activated in this test.

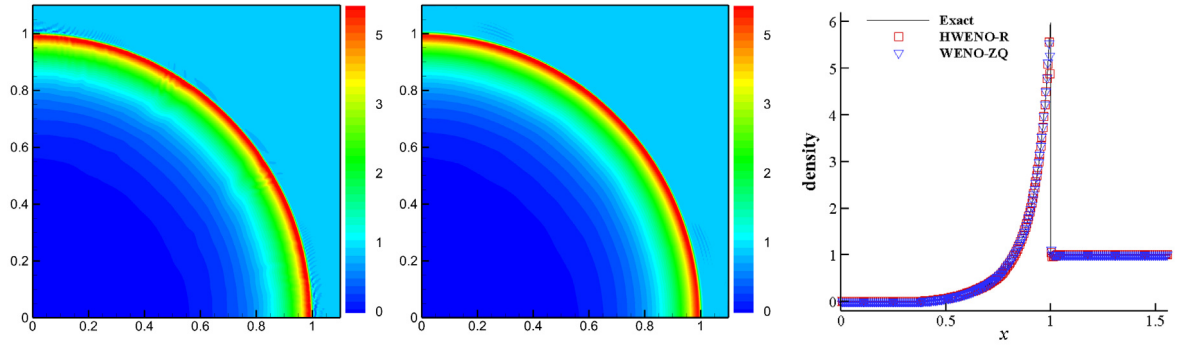

(a) HWENO-R (b) WENO-ZQ (c) Density at $x = y$

Fig. 3.14. Example 3.10. 2D Sedov problem. Contour plots of density with 40 equally spaced lines from 0.1 to 5. Meshes: 320 × 320.

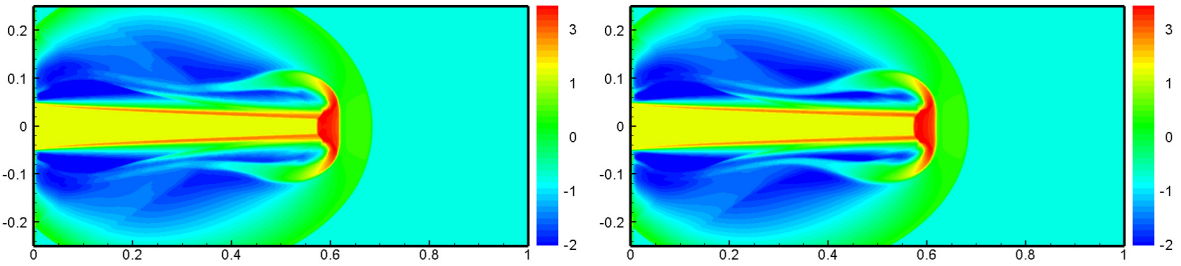

(a) HWENO-R (b) WENO-ZQ

Fig. 3.15. Example 3.11. High Mach 2000 problem. Contour plots of density with 40 equally spaced lines from −2 to 3 and scales are logarithmic. Meshes: 640 × 320.

Example 3.12. We consider a Mach 10 shock problem with shock reflection and diffraction [43]. The computational domain is a union of $[0, 1]\times[0, 1]$ and $[-1, 1]\times[1, 3]$. The initial condition is a pure right-moving Mach 10 shock, initially located at $x = \frac{1}{6}$, $y = 0$, making a 60° angle with the x-axis, that is

$$(\rho, u, v, p, \gamma) = \begin{cases} (8,\ \frac{33}{4}\sin(\frac{\pi}{3}),\ -\frac{33}{4}\cos(\frac{\pi}{3}),\ 116.5,\ 1.4), & x < \frac{1}{6} + \frac{y}{\sqrt{3}}, \\ (1.4,\ 0,\ 0,\ 1,\ 1.4), & \text{otherwise.} \end{cases}$$

The boundary conditions are set as inflow on the left, outflow on the right and bottom, and reflective on the wall $[\frac{1}{6}, 1]\times\{0\}$ and $\{1\}\times[-1, 0]$. The exact post-shock condition is posed on $[0, \frac{1}{6}]\times\{0\}$. The top boundary is the exact motion of a Mach 10 shock, which is $(\rho, u, v, p) = (8, \frac{33}{4}\sin(\frac{\pi}{3}), -\frac{33}{4}\cos(\frac{\pi}{3}), 116.5)$ for $0 \le x \le \frac{1}{6} + \frac{1+20t}{\sqrt{3}}$ and $(\rho, u, v, p) = (1.4, 0, 0, 1)$ for the rest. We show the density at the final time $T = 0.2$ for the HWENO-R and WENO-ZQ schemes in Fig. 3.16. For this challenging test, we stress the importance of PP limiters again. The HWENO-R and WENO-ZQ schemes will blow up without PP limiters. The HWENO-R scheme with PP limiters works well, and the proportion of cells that used PP limiters is 0.0012%. The total CPU time for the HWENO-R scheme is 12902.85 s, and the CPU time ratio of HWENO-R/WENO-ZQ is about 1.496. The ratio is less than that in Example 3.11, since the proportion of cells that used PP limiters is much less than that in Example 3.11. Besides, the HWENO-R scheme has more compact stencils than the WENO-ZQ scheme, and it also can capture finer structures with higher resolution, such as the roll-up phenomenons.

Example 3.13. Finally, we consider the Rayleigh–Taylor instability problem [44,45] modeled by two-dimensional compressible Euler equations with source terms, where ρ and ρv are added to the right-hand side of the third and

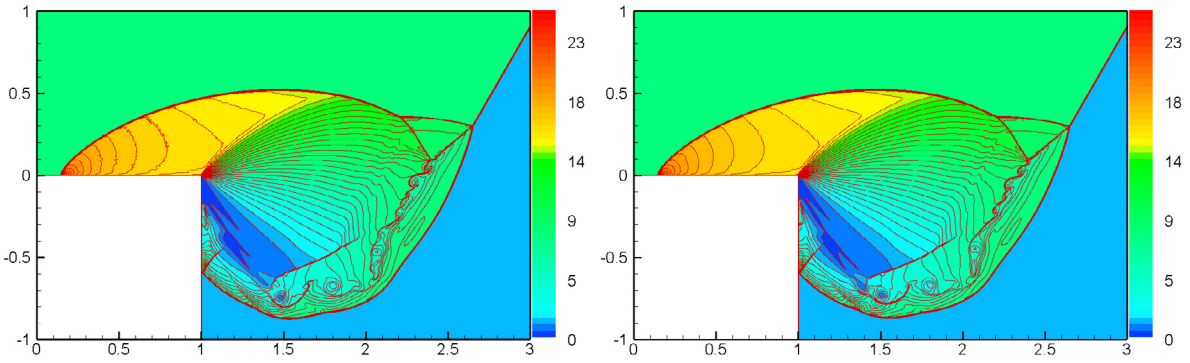

(a) HWENO-R (b) WENO-ZQ

Fig. 3.16. Example 3.12. Mach 10 shock reflection and diffraction problem. Contour plots of density with 50 equally spaced lines from 0 to 25. Meshes: 960 × 320.

fourth equations, respectively. The computational domain is $[0, 0.25] \times [0, 1]$ and the initial condition is

$$(\rho, u, v, p, \gamma) = \begin{cases} (2, 0, -0.025c \cdot \cos(8\pi x), 2y + 1, \frac{5}{3}), & 0 \le y < \frac{1}{2}, \\ (1, 0, -0.025c \cdot \cos(8\pi x), y + \frac{3}{2}, \frac{5}{3}), & \frac{1}{2} \le y \le 1, \end{cases}$$

where the sound speed $c = \sqrt{\gamma p/\rho}$. Reflective boundary conditions are imposed for the left and right. The flow values are set as $(\rho, u, v, p) = (2, 0, 0, 1)$ and $(\rho, u, v, p) = (1, 0, 0, 2.5)$ at the bottom and top boundary, respectively. We compute the time up to $T = 1.95$ and show the computational results on different meshes in Fig. 3.17 to compare the numerical dissipation of the HWENO-R and WENO-ZQ schemes. The HWENO-R and WENO-ZQ scheme capture typical flow structures well for this problem, and the results are similar to that in [46]. We observe that the resolution of solutions computed by the HWENO-R scheme exhibits better performance and dispersive behavior, having a more subtle roll-up structure than the WENO-ZQ scheme on the same meshes. Besides, the results are comparable for the HWENO-R scheme with coarser meshes (e.g., 120 × 480) and the WENO-ZQ scheme with denser meshes (e.g., 240 × 960), which both illustrate that the HWENO-R scheme has low-dissipation property. This example shows that compact reconstructions have better resolution due to less dissipation and dispersion. The analysis of spectral property for high order WENO schemes can be seen in [47], and the analysis of the dispersion and dissipation behavior for HWENO schemes is going on.

Remark 3.2. For two-dimensional high extreme problems, such as the Mach 2000 astrophysical jet flows and the shock reflection and diffraction problem, a parametrized PP flux limiter [35] is still necessary for the proposed HWENO-R and WENO-ZQ [5] schemes.

4. Concluding remarks

In this paper, we proposed a robust FD HWENO-R scheme for compressible Euler equations. The main idea is to avoid the derivative of a target cell in the flux reconstructions compared with existing FD HWENO schemes [21,26,29,31,32]. To save computational cost and control numerical spurious oscillations, all derivative values are restricted only at each Runge–Kutta time stage by a HWENO limiter, while others only use linear approximations. The proposed HWENO-R scheme has optimal fifth order accuracy and is more efficient than the HWENO-L [32] and WENO-ZQ [5] schemes. It is also more robust since it can directly simulate many challenging problems. In contrast, other HWENO schemes [21,26,29,31] need additional PP technique, and the HWENO-L scheme cannot simulate the challenging problems even using extra PP limiters in [35]. The HWENO-R scheme has higher resolutions than the WENO-ZQ scheme due to more compact stencils at the cost of solving additional derivative equations. Overall, the HWENO-R scheme can be slightly better than the WENO-ZQ scheme for resolving some fine structures at the same computational cost. For two-dimensional high extreme problems, such as the Mach

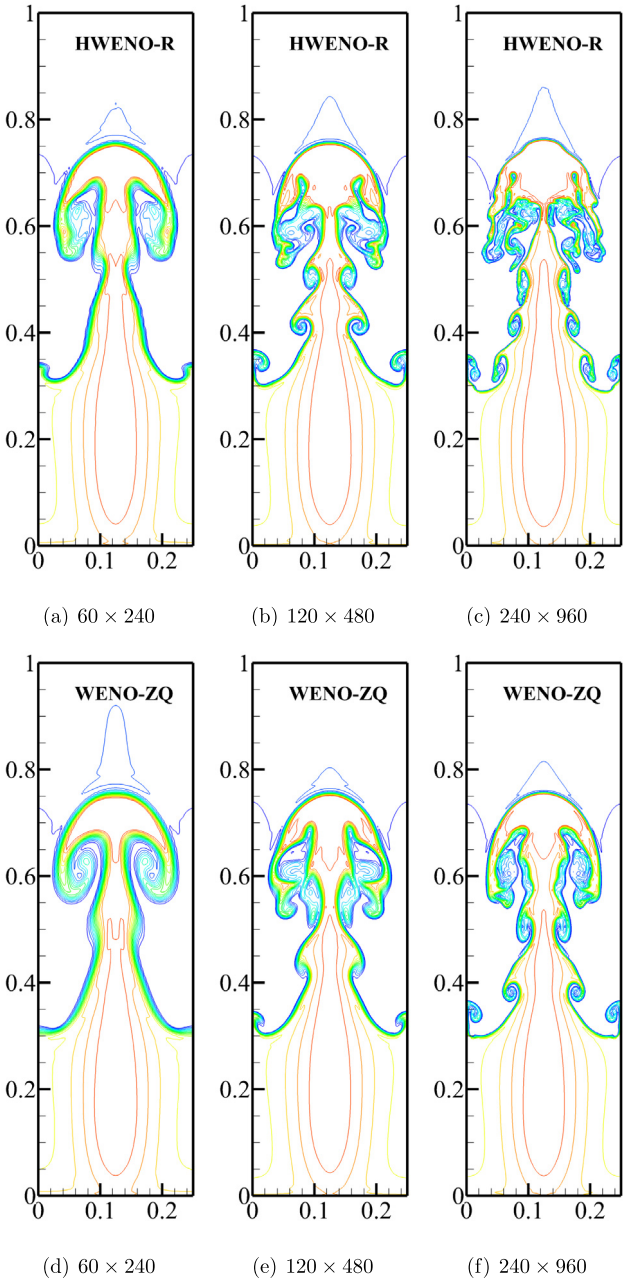

(a) 60 × 240 (b) 120 × 480 (c) 240 × 960

(d) 60 × 240 (e) 120 × 480 (f) 240 × 960

Fig. 3.17. Example 3.13. Rayleigh–Taylor instability problem. Contour plots of density with 15 equally spaced lines from 0.952269 to 2.14589.

2000 astrophysical jet flows and the shock reflection and diffraction problem, the PP limiters were activated for both the HWENO-R and WENO-ZQ schemes to avoid negative density or pressure. The PP limiters may further increase computational cost for both schemes, but they make the schemes more robust.

Declaration of competing interest

The authors declare the following financial interests/personal relationships which may be considered as potential competing interests: Chuan Fan, Tao Xiong and Jianxian Qiu reports financial support was provided by National Key

R&D Program of China (Grant Number 2022Y-FA1004500). Zhuang Zhao reports financial support was provided by Postdoctoral Science Foundation of China (Grant Number 2021M702145).

Data availability

No data was used for the research described in the article

Appendix

The two-dimensional compressible Euler equations

$$\mathbf{U}_t + \mathbf{F}(\mathbf{U})_x + \mathbf{G}(\mathbf{U})_y = 0, \tag{A.1}$$

with

$$\mathbf{U} = \begin{bmatrix} \rho \\ m \\ n \\ E \end{bmatrix}, \mathbf{F}(\mathbf{U}) = \begin{bmatrix} \rho u \\ \rho u^2 + p \\ \rho uv \\ (E+p)u \end{bmatrix}, \mathbf{G}(\mathbf{U}) = \begin{bmatrix} \rho v \\ \rho uv \\ \rho u^2 + p \\ (E+p)v \end{bmatrix},$$

where ρ is the density, $m = \rho u$ and $n = \rho v$ are the momenta, u and v are velocities along x and y directions, respectively, p is the pressure, $E = \frac{1}{2}\rho(u^2+v^2) + \frac{p}{\gamma-1}$ is the total energy. Following [21,29], we introduce two auxiliary variables $\mathbf{V} = \mathbf{U}_x$ and $\mathbf{W} = \mathbf{U}_y$ to solve

$$\begin{cases} \mathbf{U}_t + \mathbf{F}(\mathbf{U})_x + \mathbf{G}(\mathbf{U})_y = 0, \\ \mathbf{V}_t + \mathbf{H}(\mathbf{U},\mathbf{V})_x + \mathbf{R}(\mathbf{U},\mathbf{V})_y = 0, \\ \mathbf{W}_t + \mathbf{Q}(\mathbf{U},\mathbf{W})_x + \mathbf{S}(\mathbf{U},\mathbf{W})_y = 0, \end{cases} \tag{A.2}$$

where

$$\mathbf{H}(\mathbf{U},\mathbf{V}) = \mathbf{F}'(\mathbf{U})\,\mathbf{V} \quad \text{and} \quad \mathbf{R}(\mathbf{U},\mathbf{V}) = \mathbf{G}'(\mathbf{U})\,\mathbf{V},$$
$$\mathbf{Q}(\mathbf{U},\mathbf{W}) = \mathbf{G}'(\mathbf{U})\,\mathbf{W} \text{ and } \quad \mathbf{S}(\mathbf{U},\mathbf{W}) = \mathbf{G}'(\mathbf{U})\,\mathbf{W},$$

with Jacobian matrix $\mathbf{F}'(\mathbf{U}) = \partial\mathbf{F}(\mathbf{U})/\partial\mathbf{U}$, which has four eigenvalues $u-c, u, u, u+c$, and Jacobian matrix $\mathbf{G}'(\mathbf{U}) = \partial\mathbf{G}(\mathbf{U})/\partial\mathbf{U}$ with $v-c, v, v, v+c$, where the speed of sound $c = \sqrt{\gamma p/\rho}$. A conservative semi-discrete FD HWENO scheme for (A.2) is defined as

$$\begin{cases} \dfrac{\mathrm{d}\mathbf{U}_{i,j}(t)}{\mathrm{d}t} = -\dfrac{1}{\Delta x}(\widehat{\mathbf{F}}_{i+\frac{1}{2},j} - \widehat{\mathbf{F}}_{i-\frac{1}{2},j}) - \dfrac{1}{\Delta y}(\widehat{\mathbf{G}}_{i,j+\frac{1}{2}} - \widehat{\mathbf{G}}_{i,j-\frac{1}{2}}), \\ \dfrac{\mathrm{d}\mathbf{V}_{i,j}(t)}{\mathrm{d}t} = -\dfrac{1}{\Delta x}(\widehat{\mathbf{H}}_{i+\frac{1}{2},j} - \widehat{\mathbf{H}}_{i-\frac{1}{2},j}) - \dfrac{1}{\Delta y}(\widehat{\mathbf{R}}_{i,j+\frac{1}{2}} - \widehat{\mathbf{R}}_{i,j-\frac{1}{2}}), \\ \dfrac{\mathrm{d}\mathbf{W}_{i,j}(t)}{\mathrm{d}t} = -\dfrac{1}{\Delta x}(\widehat{\mathbf{Q}}_{i+\frac{1}{2},j} - \widehat{\mathbf{Q}}_{i-\frac{1}{2},j}) - \dfrac{1}{\Delta y}(\widehat{\mathbf{S}}_{i,j+\frac{1}{2}} - \widehat{\mathbf{S}}_{i,j-\frac{1}{2}}), \end{cases} \tag{A.3}$$

where $\widehat{\mathbf{F}}_{i+\frac{1}{2},j}$, $\widehat{\mathbf{H}}_{i+\frac{1}{2},j}$, $\widehat{\mathbf{Q}}_{i+\frac{1}{2},j}$, $\widehat{\mathbf{G}}_{i,j+\frac{1}{2}}$, $\widehat{\mathbf{R}}_{i,j+\frac{1}{2}}$ and $\widehat{\mathbf{S}}_{i,j+\frac{1}{2}}$ are numerical fluxes.

For the 2D HWENO scheme (A.3), a parametrized PP flux limiter is applied to the main variable $\mathbf{U}$ at the final stage for a high order multi-stage RK scheme which is rewritten as

$$\mathbf{U}^{n+1}_{i,j} = \mathbf{U}^{n}_{i,j} - \lambda_x(\widehat{\mathbf{F}}^{\mathrm{RK}}_{i+\frac{1}{2},j} - \widehat{\mathbf{F}}^{\mathrm{RK}}_{i-\frac{1}{2},j}) - \lambda_y(\widehat{\mathbf{G}}^{\mathrm{RK}}_{i,j+\frac{1}{2}} - \widehat{\mathbf{G}}^{\mathrm{RK}}_{i,j-\frac{1}{2}}), \tag{A.4}$$

where numerical fluxes $\widehat{\mathbf{F}}^{\mathrm{RK}}_{i+\frac{1}{2},j}$ and $\widehat{\mathbf{G}}^{\mathrm{RK}}_{i,j+\frac{1}{2}}$ are convex combinations of corresponding numerical fluxes from the multi-stage RK method for each component. $\lambda_x = \Delta t/\Delta x$ and $\lambda_y = \Delta t/\Delta y$. Denote $\widehat{\mathbf{F}}^{\mathrm{RK}}_{i+\frac{1}{2},j} = (\widehat{f}^{\rho}_{i+\frac{1}{2},j}, \widehat{f}^{m}_{i+\frac{1}{2},j}, \widehat{f}^{n}_{i+\frac{1}{2},j}, \widehat{f}^{E}_{i+\frac{1}{2},j})^T$ and $\widehat{\mathbf{G}}^{\mathrm{RK}}_{i,j+\frac{1}{2}} = (\widehat{g}^{\rho}_{i,j+\frac{1}{2}}, \widehat{g}^{m}_{i,j+\frac{1}{2}}, \widehat{g}^{n}_{i,j+\frac{1}{2}}, \widehat{g}^{E}_{i,j+\frac{1}{2}})^T$. For maintaining the PP property of scheme (A.4), we modify $\widehat{\mathbf{F}}^{\mathrm{RK}}_{i+\frac{1}{2},j}$ and $\widehat{\mathbf{G}}^{\mathrm{RK}}_{i,j+\frac{1}{2}}$ by

$$\begin{aligned} \widetilde{\mathbf{F}}^{\mathrm{RK}}_{i+\frac{1}{2},j} &= \theta_{i+\frac{1}{2},j}(\widehat{\mathbf{F}}^{\mathrm{RK}}_{i+\frac{1}{2},j} - \widehat{\mathbf{f}}_{i+\frac{1}{2},j}) + \widehat{\mathbf{f}}_{i+\frac{1}{2},j}, \\ \widetilde{\mathbf{G}}^{\mathrm{RK}}_{i,j+\frac{1}{2}} &= \theta_{i,j+\frac{1}{2}}(\widehat{\mathbf{G}}^{\mathrm{RK}}_{i,j+\frac{1}{2}} - \widehat{\mathbf{g}}_{i,j+\frac{1}{2}}) + \widehat{\mathbf{g}}_{i,j+\frac{1}{2}}, \end{aligned} \tag{A.5}$$

such that for the new updated scheme of $\mathbf{U}_{i,j}^{n+1}$,

$$\mathbf{U}_{i,j}^{n+1} = \mathbf{U}_{i,j}^{n} - \lambda_x(\widetilde{\mathbf{F}}_{i+\frac{1}{2},j}^{\mathrm{RK}} - \widetilde{\mathbf{F}}_{i-\frac{1}{2},j}^{\mathrm{RK}}) - \lambda_y(\widetilde{\mathbf{G}}_{i,j+\frac{1}{2}}^{\mathrm{RK}} - \widetilde{\mathbf{G}}_{i,j-\frac{1}{2}}^{\mathrm{RK}}), \tag{A.6}$$

we have $\rho_{i,j}^{n+1} > 0$ and $p_{i,j}^{n+1} > 0$ for all i, j. Here $\widehat{\mathbf{f}}_{i+\frac{1}{2},j} = (f_{i+\frac{1}{2},j}^{\rho}, f_{i+\frac{1}{2},j}^{m}, f_{i+\frac{1}{2},j}^{n}, f_{i+\frac{1}{2},j}^{E})^T$ and $\widehat{\mathbf{g}}_{i,j+\frac{1}{2}} = (g_{i,j+\frac{1}{2}}^{\rho}, g_{i,j+\frac{1}{2}}^{m}, g_{i,j+\frac{1}{2}}^{n}, g_{i,j+\frac{1}{2}}^{E})^T$ similarly can be taken as the first order monotone Lax–Friedrichs fluxes

$$\begin{aligned}
\widehat{\mathbf{f}}_{i+\frac{1}{2},j} &= \widehat{\mathbf{f}}(\mathbf{U}_{i,j}, \mathbf{U}_{i+1,j}) = \frac{1}{2}[\mathbf{f}(\mathbf{U}_{i,j}) + \mathbf{f}(\mathbf{U}_{i+1,j}) - \alpha_x(\mathbf{U}_{i+1,j} - \mathbf{U}_{i,j})],\\
\widehat{\mathbf{g}}_{i,j+\frac{1}{2}} &= \widehat{\mathbf{f}}(\mathbf{U}_{i,j}, \mathbf{U}_{i,j+1}) = \frac{1}{2}[\mathbf{g}(\mathbf{U}_{i,j}) + \mathbf{g}(\mathbf{U}_{i,j+1}) - \alpha_y(\mathbf{U}_{i,j+1} - \mathbf{U}_{i,j})],
\end{aligned}$$

where $\alpha_x = \||u| + c\|_\infty$ and $\alpha_y = \||v| + c\|_\infty$. Let $\widehat{\mathbf{U}}_{i,j}^{n+1} = (\widehat{\rho}_{i,j}^{n+1}, \widehat{m}_{i,j}^{n+1}, \widehat{n}_{i,j}^{n+1}, \widehat{E}_{i,j}^{n+1})^T$, which is updated by the first order numerical fluxes,

$$\widehat{\mathbf{U}}_{i,j}^{n+1} = \mathbf{U}_{i,j}^{n} - \lambda_x(\widehat{\mathbf{f}}_{i+\frac{1}{2},j} - \widehat{\mathbf{f}}_{i-\frac{1}{2},j}) - \lambda_y(\widehat{\mathbf{g}}_{i,j+\frac{1}{2}} - \widehat{\mathbf{g}}_{i,j-\frac{1}{2}}), \tag{A.7}$$

then $\widehat{\rho}_{i,j}^{n+1} > 0$ and $\widehat{p}_{i,j}^{n+1} = p(\widehat{\mathbf{U}}_{i,j}^{n+1}) > 0$.

Define two small positive numbers $\varepsilon_\rho = \min_{i,j}\{\widehat{\rho}_{i,j}^{n+1}, 10^{-13}\} > 0$ and $\varepsilon_p = \min_{i,j}\{\widehat{p}_{i,j}^{n+1}, 10^{-13}\} > 0$. To obtain a PP scheme (A.6), we look for four parameters $(\Lambda_{L,I_{i,j}}, \Lambda_{R,I_{i,j}}, \Lambda_{D,I_{i,j}}, \Lambda_{U,I_{i,j}})$, such that for any $\theta_{i-\frac{1}{2},j} \in [0, \Lambda_{L,I_{i,j}}]$, $\theta_{i+\frac{1}{2},j} \in [0, \Lambda_{R,I_{i,j}}]$, $\theta_{i,j-\frac{1}{2}} \in [0, \Lambda_{D,I_{i,j}}]$, and $\theta_{i,j+\frac{1}{2}} \in [0, \Lambda_{U,I_{i,j}}]$, the scheme (A.6) with updated $\mathbf{U}_{i,j}^{n+1}$ will have $\rho_{i,j}^{n+1} > 0$ and $p_{i,j}^{n+1} > 0$ for all i, j. The procedure is bellowed.

- **Step I. To obtain a positive density.** For the density, we consider the first component of (A.6), which requires

$$\rho_{i,j}^{n+1} = \rho_{i,j}^{n} - \lambda_x(\widetilde{f}_{i+\frac{1}{2},j}^{\rho} - \widetilde{f}_{i-\frac{1}{2},j}^{\rho}) - \lambda_y(\widetilde{g}_{i,j+\frac{1}{2}}^{\rho} - \widetilde{g}_{i,j-\frac{1}{2}}^{\rho}) \geq \varepsilon_\rho > 0.$$

  It can be revised as

$$\theta_{i-\frac{1}{2},j} f_{i-\frac{1}{2},j} + \theta_{i+\frac{1}{2},j} f_{i+\frac{1}{2},j} + \theta_{i,j-\frac{1}{2}} f_{i,j-\frac{1}{2}} + \theta_{i,j+\frac{1}{2}} f_{i,j+\frac{1}{2}} \geq \varepsilon_\rho - \widehat{\rho}_{i,j}^{n+1}, \tag{A.8}$$

  with

$$\begin{aligned}
f_{i-\frac{1}{2},j} &= \lambda_x(\widehat{f}_{i-\frac{1}{2},j}^{\rho} - f_{i-\frac{1}{2},j}^{\rho}), \quad & f_{i+\frac{1}{2},j} &= -\lambda_x(\widehat{f}_{i+\frac{1}{2},j}^{\rho} - f_{i+\frac{1}{2},j}^{\rho}),\\
f_{i,j-\frac{1}{2}} &= \lambda_y(\widehat{g}_{i,j-\frac{1}{2}}^{\rho} - g_{i,j-\frac{1}{2}}^{\rho}), \quad & f_{i,j+\frac{1}{2}} &= -\lambda_y(\widehat{g}_{i,j+\frac{1}{2}}^{\rho} - g_{i,j+\frac{1}{2}}^{\rho}).
\end{aligned} \tag{A.9}$$

  First we find $(\Lambda_{L,I_{i,j}}^{\rho}, \Lambda_{R,I_{i,j}}^{\rho}, \Lambda_{D,I_{i,j}}^{\rho}, \Lambda_{U,I_{i,j}}^{\rho})$, such that (A.8) holds for any $\theta_{i-\frac{1}{2},j} \in [0, \Lambda_{L,I_{i,j}}^{\rho}]$, $\theta_{i+\frac{1}{2},j} \in [0, \Lambda_{R,I_{i,j}}^{\rho}]$, $\theta_{i,j-\frac{1}{2}} \in [0, \Lambda_{D,I_{i,j}}^{\rho}]$, and $\theta_{i,j+\frac{1}{2}} \in [0, \Lambda_{U,I_{i,j}}^{\rho}]$. The four parameters $(\Lambda_{L,I_{i,j}}^{\rho}, \Lambda_{R,I_{i,j}}^{\rho}, \Lambda_{D,I_{i,j}}^{\rho}, \Lambda_{U,I_{i,j}}^{\rho})$ can be determined by the sign of four local values $f_{i-\frac{1}{2},j}$, $f_{i+\frac{1}{2},j}$, $f_{i,j-\frac{1}{2}}$, and $f_{i,j+\frac{1}{2}}$, seen in [48]. We omit them to save space.
- **Step II. To obtain a positive pressure.** For the pressure, the requirement is

$$p_{i,j}^{n+1} = p(\mathbf{U}_{i,j}^{n+1}) = (\gamma - 1)\left(E_{i,j}^{n+1} - \frac{1}{2}\frac{(m_{i,j}^{n+1})^2 + (n_{i,j}^{n+1})^2}{\rho_{i,j}^{n+1}}\right) \geq \varepsilon_p > 0, \tag{A.10}$$

  $p_{i,j}^{n+1} = p_{i,j}^{n+1}(\theta_{i-\frac{1}{2},j}, \theta_{i+\frac{1}{2},j}, \theta_{i,j-\frac{1}{2}}, \theta_{i,j+\frac{1}{2}})$. We now look for $(\Lambda_{L,I_{i,j}}, \Lambda_{R,I_{i,j}}, \Lambda_{D,I_{i,j}}, \Lambda_{U,I_{i,j}})$, within the regions $\mathcal{S}_\rho = [0, \Lambda_{L,I_{i,j}}^{\rho}] \times [0, \Lambda_{R,I_{i,j}}^{\rho}] \times [0, \Lambda_{L,I_{i,j}}^{\rho}] \times [0, \Lambda_{D,I_{i,j}}^{\rho}]$, such that (A.10) holds for any $\theta_{i-\frac{1}{2},j} \in [0, \Lambda_{L,I_{i,j}}]$, $\theta_{i+\frac{1}{2},j} \in [0, \Lambda_{R,I_{i,j}}]$, $\theta_{i,j-\frac{1}{2}} \in [0, \Lambda_{D,I_{i,j}}]$, and $\theta_{i,j+\frac{1}{2}} \in [0, \Lambda_{U,I_{i,j}}]$. To find the largest possible value of $(\Lambda_{L,I_{i,j}}, \Lambda_{R,I_{i,j}}, \Lambda_{D,I_{i,j}}, \Lambda_{U,I_{i,j}})$ within the regions $\mathcal{S}_\rho$, the procedure is given as follows:

  1. We define the 16 vertices of $\mathcal{S}_\rho$ as $A^{k_1,k_2,k_3,k_4} = (k_1\Lambda_{L,I_{i,j}}^{\rho}, k_2\Lambda_{R,I_{i,j}}^{\rho}, k_3\Lambda_{D,I_{i,j}}^{\rho}, k_4\Lambda_{U,I_{i,j}}^{\rho})$, with $k_1, k_2, k_3, k_4 \in \{0, 1\}$. If $p(A^{(k_1,k_2,k_3,k_4)}) \geq \varepsilon_p$, we let $B^{(k_1,k_2,k_3,k_4)} = A^{(k_1,k_2,k_3,k_4)}$; Otherwise, we find a scaling parameter r, such that $p(rA^{(k_1,k_2,k_3,k_4)}) \geq \varepsilon_p$ and we take $B^{(k_1,k_2,k_3,k_4)} = rA^{(k_1,k_2,k_3,k_4)}$. r is obtained by solving (A.10) as equality, which is still a quadratic equation of r.

Algorithm A.1: Implementation of 2D PP flux limiter

Input: point values $\lambda_x, \lambda_y, \gamma, \mathbf{U}_{i,j}, \hat{\mathbf{f}}_{i\pm\frac{1}{2},j}, \hat{\mathbf{g}}_{i,j\pm\frac{1}{2}}, \widehat{\mathbf{F}}^{\mathrm{RK}}_{i\pm\frac{1}{2},j}, \widehat{\mathbf{G}}^{\mathrm{RK}}_{i,j\pm\frac{1}{2}}$.

Output: $\theta_{i+\frac{1}{2},j}$ and $\theta_{i,j+\frac{1}{2}}$.

Compute $\widehat{\mathbf{U}}_{i,j}$ and $\hat{p}_{i,j}$ at initial time, and define two small parameters $\{\epsilon_\rho, \epsilon_p\}$, namely,

$\epsilon_\rho = \min\{\min_{i,j}\{\hat{\rho}_{i,j}\}, 10^{-13}\}$, $\epsilon_p = \min\{\min_{i,j}\{\hat{p}_{i,j}\}, 10^{-13}\}$, $i = 0, \ldots, N_x$, $j = 0, \ldots, N_y$.

for $i = 0, \ldots, N_x,\ j = 0, \ldots, N_y,$ **do**

$\widehat{\mathbf{U}}_{i,j} = \mathbf{U}_{i,j} - \lambda_x(\hat{\mathbf{f}}_{i+\frac{1}{2},j} - \hat{\mathbf{f}}_{i-\frac{1}{2},j}) - \lambda_y(\hat{\mathbf{g}}_{i,j+\frac{1}{2}} - \widehat{\mathbf{g}}_{i,j-\frac{1}{2}})$,

$\hat{p}_{i,j} = p(\widehat{\mathbf{U}}_{i,j}) = (\gamma - 1)(\hat{E}_{i,j} - \frac{1}{2}(\hat{m}^2_{i,j} + \hat{n}^2_{i,j})/\hat{\rho}_{i,j})$.

Step I. Maintain the positive density.

for $i = 0, \ldots, N_x,\ j = 0, \ldots, N_y,$ **do**

Let $g_m(i, j, 1:4) = (\Lambda^\rho_{L,I_{i,j}}, \Lambda^\rho_{R,I_{i,j}}, \Lambda^\rho_{D,I_{i,j}}, \Lambda^\rho_{U,I_{i,j}}) = (1, 1, 1, 1)$ and $I_s(1:4) = 0$.

$f(1) = \lambda_x(\hat{f}^\rho_{i-\frac{1}{2},j} - f^\rho_{i-\frac{1}{2},j})$,

$f(2) = -\lambda_x(\hat{f}^\rho_{i+\frac{1}{2},j} - f^\rho_{i+\frac{1}{2},j})$,

$f(3) = \lambda_y(\hat{g}^\rho_{i,j-\frac{1}{2}} - g^\rho_{i,j-\frac{1}{2}})$,

$f(4) = -\lambda_y(\hat{g}^\rho_{i,j+\frac{1}{2}} - g^\rho_{i,j+\frac{1}{2}})$.

for $k = 1, \ldots, 4,$ **do**

If $f(k) < 0$, then let $I_s(k) = 1$.

$f_s = I_s(1) \cdot f(1) + I_s(2) \cdot f(2) + I_s(3) \cdot f(3) + I_s(4) \cdot f(4)$.

for $k = 1, \ldots, 4,$ **do**

If $f(k) = 1$, then let $g_m(i, j, k) = \min(\frac{\epsilon_\rho - \hat{\rho}_{i,j}}{f_s}, 1)$.

Step II. Maintain the positive pressure.

for $i = 0, \ldots, N_x,\ j = 0, \ldots, N_y,$ **do**

$r(0:1, 0:1, 0:1, 0:1) = 1$.

for $k_1, k_2, k_3, k_4 = 0, 1,$ **do**

$\mathbf{f}_1 = k_1 g_m(i, j, 1)(\widehat{\mathbf{F}}^{\mathrm{RK}}_{i-\frac{1}{2},j} - \hat{\mathbf{f}}_{i-\frac{1}{2},j})$,

$\mathbf{f}_2 = k_2 g_m(i, j, 2)(\widehat{\mathbf{F}}^{\mathrm{RK}}_{i+\frac{1}{2},j} - \hat{\mathbf{f}}_{i+\frac{1}{2},j})$,

$\mathbf{f}_3 = k_3 g_m(i, j, 3)(\widehat{\mathbf{G}}^{\mathrm{RK}}_{i,j-\frac{1}{2}} - \hat{\mathbf{g}}_{i,j-\frac{1}{2}})$,

$\mathbf{f}_4 = k_4 g_m(i, j, 4)(\widehat{\mathbf{G}}^{\mathrm{RK}}_{i,j+\frac{1}{2}} - \hat{\mathbf{g}}_{i,j+\frac{1}{2}})$,

$\widehat{\mathbf{U}}^{new}_{i,j} = \widehat{\mathbf{U}}_{i,j} - \lambda_x(\mathbf{f}_2 - \mathbf{f}_1) - \lambda_y(\mathbf{f}_4 - \mathbf{f}_3)$.

Find $r(k_1, k_2, k_3, k_4)$, such that $p^{new}_{i,j} = p(\widehat{\mathbf{U}}^{new}_{i,j}) \geq \epsilon_p > 0$.

$g_m(i, j, 1) = g_m(i, j, 1) \cdot \min\{1, r(1, 0:1, 0:1, 0:1)\}$,

$g_m(i, j, 2) = g_m(i, j, 2) \cdot \min\{1, r(0:1, 1, 0:1, 0:1)\}$,

$g_m(i, j, 3) = g_m(i, j, 3) \cdot \min\{1, r(0:1, 0:1, 1, 0:1)\}$,

$g_m(i, j, 4) = g_m(i, j, 4) \cdot \min\{1, r(0:1, 0:1, 0:1, 1)\}$.

Step III. Take the limiting parameter as $\theta_{i+\frac{1}{2},j} = \min\{g_m(i+1, j, 1), g_m(i, j, 2)\}$, $\theta_{i,j+\frac{1}{2}} = \min\{g_m(i, j+1, 3), g_m(i, j, 4)\}$.

2. After obtaining $B^{(k_1,k_2,k_3,k_4)}$ for $k_1, k_2, k_3, k_4 \in \{0, 1\}$, we let

$$\Lambda_{L,I_{i,j}} = \min_{k_2,k_3,k_4\in\{0,1\}} B^{(1,k_2,k_3,k_4)}, \quad \Lambda_{R,I_{i,j}} = \min_{k_1,k_3,k_4\in\{0,1\}} B^{(k_1,1,k_3,k_4)},$$
$$\Lambda_{D,I_{i,j}} = \min_{k_1,k_2,k_4\in\{0,1\}} B^{(k_1,k_2,1,k_4)}, \quad \Lambda_{U,I_{i,j}} = \min_{k_1,k_2,k_3\in\{0,1\}} B^{(k_1,k_2,k_3,1)}.$$

The four parameters define the largest tesseract within four-dimensional polyhedra formed by the vertices of $\{B^{(k_1,k_2,k_3,k_4)} : k_1, k_2, k_3, k_4 \in \{0, 1\}\}$.

- **Step III.** Finally the local parameters are taken as $\theta_{i+\frac{1}{2},j} = \min\{\Lambda_{R,I_{i,j}}, \Lambda_{L,I_{i+1,j}}\}$ and $\theta_{i,j+\frac{1}{2}} = \min\{\Lambda_{U,I_{i,j}}, \Lambda_{D,I_{i,j+1}}\}$.

The above procedure can ensure the PP property of density and pressure, but it is a sufficient procedure, so the PP limiters might be activated even without negative density and pressure. For preserving high order accuracy, it relies on numerical verification [35]. The simplified implementations of the 2D PP limiters are given in Algorithm A.1.

References

[1] Z. Xu, X. Zhang, Bound-preserving high-order schemes, in: Handbook of Numerical Analysis, Vol. 18, 2017, pp. 81–102.
[2] G.-S. Jiang, C.-W. Shu, Efficient implementation of weighted ENO schemes, J. Comput. Phys. 126 (1) (1996) 202–228.
[3] R. Borges, M. Carmona, B. Costa, W.S. Don, An improved weighted essentially non-oscillatory scheme for hyperbolic conservation laws, J. Comput. Phys. 227 (6) (2008) 3191–3211.
[4] M. Castro, B. Costa, W.S. Don, High order weighted essentially non-oscillatory WENO-Z schemes for hyperbolic conservation laws, J. Comput. Phys. 230 (5) (2011) 1766–1792.
[5] J. Zhu, J. Qiu, A new fifth order finite difference WENO scheme for solving hyperbolic conservation laws, J. Comput. Phys. 318 (2016) 110–121.
[6] J. Zhu, C.-W. Shu, A new type of multi-resolution WENO schemes with increasingly higher order of accuracy, J. Comput. Phys. 375 (2018) 659–683.
[7] X.-D. Liu, S. Osher, T. Chan, Weighted essentially non-oscillatory schemes, J. Comput. Phys. 115 (1) (1994) 200–212.
[8] C. Hu, C.-W. Shu, Weighted essentially non-oscillatory schemes on triangular meshes, J. Comput. Phys. 150 (1) (1999) 97–127.
[9] J. Shi, C. Hu, C.-W. Shu, A technique of treating negative weights in WENO schemes, J. Comput. Phys. 175 (1) (2002) 108–127.
[10] Y.-T. Zhang, C.-W. Shu, Third order WENO scheme on three dimensional tetrahedral meshes, Commun. Comput. Phys. 5 (2–4) (2009) 836–848.
[11] J. Zhu, C.-W. Shu, A new type of multi-resolution WENO schemes with increasingly higher order of accuracy on triangular meshes, J. Comput. Phys. 392 (2019) 19–33.
[12] B. Cockburn, C.W. Shu, TVB Runge-Kutta local projection discontinuous Galerkin finite element method for conservation laws. II. General framework, Math. Comp. 52 (186) (1989) 411.
[13] B. Cockburn, S.-Y. Lin, C.-W. Shu, TVB Runge-Kutta local projection discontinuous Galerkin finite element method for conservation laws III: one-dimensional systems, J. Comput. Phys. 84 (1) (1989) 90–113.
[14] B. Cockburn, S. Hou, C.-W. Shu, The Runge-Kutta local projection discontinuous Galerkin finite element method for conservation laws. IV. The multidimensional case, Math. Comp. 54 (190) (1990) 545–581.
[15] B. Cockburn, C.-W. Shu, The Runge-Kutta local projection-discontinuous-Galerkin finite element method for scalar conservation laws, ESAIM Math. Model. Numer. Anal. 25 (3) (1991) 337–361.
[16] B. Cockburn, C.-W. Shu, The Runge–Kutta discontinuous Galerkin method for conservation laws V: multidimensional systems, J. Comput. Phys. 141 (2) (1998) 199–224.
[17] J. Qiu, C.-W. Shu, Hermite WENO schemes and their application as limiters for Runge-Kutta discontinuous Galerkin method: one-dimensional case, J. Comput. Phys. 193 (1) (2004) 115–135, http://dx.doi.org/10.1016/j.jcp.2003.07.026, URL.
[18] J. Qiu, C.-W. Shu, Hermite WENO schemes and their application as limiters for Runge-Kutta discontinuous Galerkin method II: Two dimensional case, Comput. & Fluids 34 (6) (2005) 642–663, http://dx.doi.org/10.1016/j.compfluid.2004.05.005.
[19] J. Zhu, J. Qiu, A class of the fourth order finite volume Hermite weighted essentially non-oscillatory schemes, Sci. China Ser. A Math. 51 (8) (2008) 1549–1560, http://dx.doi.org/10.1007/s11425-008-0105-0.
[20] G. Capdeville, A Hermite upwind WENO scheme for solving hyperbolic conservation laws, J. Comput. Phys. 227 (4) (2008) 2430–2454.
[21] H. Liu, J. Qiu, Finite difference Hermite WENO schemes for hyperbolic conservation laws, J. Sci. Comput. 63 (2) (2015) 548–572, http://dx.doi.org/10.1007/s10915-014-9905-2, URL.
[22] X.Y. Hu, N. Adams, C.-W. Shu, Positivity-preserving method for high-order conservative schemes solving compressible Euler equations, J. Comput. Phys. 242 (2013) 169–180, http://dx.doi.org/10.1016/j.jcp.2013.01.024.
[23] X. Zhang, C.-W. Shu, On positivity-preserving high order discontinuous Galerkin schemes for compressible Euler equations on rectangular meshes, J. Comput. Phys. 229 (23) (2010) 8918–8934, http://dx.doi.org/10.1016/j.jcp.2010.08.016.
[24] X. Cai, X. Zhang, J. Qiu, Positivity-preserving high order finite volume HWENO schemes for compressible Euler equations, J. Sci. Comput. 68 (2) (2016) 464–483.

[25] Z. Tao, F. Li, J. Qiu, High-order central Hermite WENO schemes on staggered meshes for hyperbolic conservation laws, J. Comput. Phys. 281 (2015) 148–176, http://dx.doi.org/10.1016/j.jcp.2014.10.027.
[26] Y.H. Zahran, A.H. Abdalla, Seventh order Hermite WENO scheme for hyperbolic conservation laws, Comput. & Fluids (2016) 66–80.
[27] Z. Ma, S.-P. Wu, HWENO schemes based on compact difference for hyperbolic conservation laws, J. Sci. Comput. 76 (2) (2018) 1301–1325.
[28] Z. Zhao, Y. Chen, J. Qiu, A hybrid Hermite WENO scheme for hyperbolic conservation laws, J. Comput. Phys. 405 (2020) 109175.
[29] Z. Zhao, Y.-T. Zhang, J. Qiu, A modified fifth order finite difference Hermite WENO scheme for hyperbolic conservation laws, J. Sci. Comput. 85 (2) (2020) 1–22.
[30] I. Wibisono, Yanuar, E.A. Kosasih, Fifth-order Hermite targeted essentially non-oscillatory schemes for hyperbolic conservation laws, J. Sci. Comput. 87 (3) (2021) 1–23.
[31] J. Li, C.-W. Shu, J. Qiu, Multi-resolution HWENO schemes for hyperbolic conservation laws, J. Comput. Phys. 446 (2021) 110653.
[32] M. Zhang, Z. Zhao, A fifth-order finite difference HWENO scheme combined with limiter for hyperbolic conservation laws, J. Comput. Phys. 472 (2023) 111676.
[33] C. Fan, X. Zhang, J. Qiu, Positivity-preserving high order finite volume hybrid Hermite WENO scheme for compressible Navier-Stokes equations, J. Comput. Phys. 445 (2021) 110596, http://dx.doi.org/10.1016/j.jcp.2021.110596, URL https://www.sciencedirect.com/science/article/pii/S0021999121004915.
[34] X. Zhang, On positivity-preserving high order discontinuous Galerkin schemes for compressible Navier-Stokes equations, J. Comput. Phys. 328 (2017) 301–343.
[35] T. Xiong, J.-M. Qiu, Z. Xu, Parametrized positivity preserving flux limiters for the high order finite difference WENO scheme solving compressible Euler equations, J. Sci. Comput. 67 (3) (2016) 1066–1088.
[36] X. Zhang, C.-W. Shu, Positivity-preserving high order finite difference WENO schemes for compressible Euler equations, J. Comput. Phys. 231 (5) (2012) 2245–2258, http://dx.doi.org/10.1016/j.jcp.2011.11.020.
[37] L.I. Sedov, Similarity and Dimensional Methods in Mechanics, Academic Press, New York, 1959.
[38] V.P. Korobeinikov, Problems of Point Blast Theory, American Institute of Physics, College Park, 1991.
[39] T. Linde, P. Roe, Robust Euler codes, AIAA paper-97-2098, in: 13th Computational Fluid Dynamics Conference, Snowmass Village, CO, 1997.
[40] Y. Ha, C.L. Gardner, A. Gelb, C.-W. Shu, Numerical simulation of high Mach number astrophysical jets with radiative cooling, J. Sci. Comput. 24 (1) (2005) 29–44.
[41] Y. Ha, C.L. Gardner, Positive scheme numerical simulation of high Mach number astrophysical jets, J. Sci. Comput. 34 (3) (2008) 247–259.
[42] C.L. Gardner, S.J. Dwyer, Numerical simulation of the XZ Tauri supersonic astrophysical jet, Acta Math. Sci. 29 (6) (2009) 1677–1683.
[43] C. Fan, X. Zhang, J. Qiu, Positivity-preserving high order finite difference WENO schemes for compressible Navier-Stokes equations, J. Comput. Phys. 467 (2022) 111446, http://dx.doi.org/10.1016/j.jcp.2022.111446, URL https://www.sciencedirect.com/science/article/pii/S0021999122005083.
[44] J. Shi, Y.-T. Zhang, C.-W. Shu, Resolution of high order WENO schemes for complicated flow structures, J. Comput. Phys. 186 (2) (2003) 690–696.
[45] Y.-T. Zhang, J. Shi, C.-W. Shu, Y. Zhou, Numerical viscosity and resolution of high-order weighted essentially nonoscillatory schemes for compressible flows with high Reynolds numbers, Phys. Rev. E 68 (4) (2003) 046709.
[46] Z. Wang, J. Zhu, C. Wang, N. Zhao, An efficient hybrid multi-resolution WCNS scheme for solving compressible flows, J. Comput. Phys. 477 (2023) 111877.
[47] S. Pirozzoli, On the spectral properties of shock-capturing schemes, J. Comput. Phys. 219 (2) (2006) 489–497.
[48] T. Xiong, J.-M. Qiu, Z. Xu, A parametrized maximum principle preserving flux limiter for finite difference RK-WENO schemes with applications in incompressible flows, J. Comput. Phys. 252 (2013) 310–331.